Insights into the dynamics of conical breakdown modes in coaxial swirling flow field

Kuppuraj Rajamanickam[1] and Saptarshi Basu[1,†]

[1]Department of Mechanical Engineering, Indian Institute of Science, Bangalore-560012, India

The main idea of this paper is to understand the fundamental vortex breakdown mechanisms in the coaxial swirling flow field. In particular, the interaction dynamics of the flow field is meticulously addressed with the help of high fidelity laser diagnostic tools. Time-resolved particle image velocimetry (PIV) ($\sim$1500 frames s^{-1}) is employed in y–r and multiple r–θ planes to precisely delineate the flow dynamics. Experiments are carried out for three sets of co-annular flow Reynolds number $Re_a = 4896$, $10\,545$, $17\,546$. Furthermore, for each Re_a condition, the swirl number 'S_G' is varied independently from $0 \leqslant S_G \leqslant 3$. The global evolution of flow field across various swirl numbers is presented using the time-averaged PIV data. Three distinct forms of vortex breakdown namely, pre-vortex breakdown (PVB), central toroidal recirculation zone (CTRZ; axisymmetric toroidal bubble type breakdown) and sudden conical breakdown are witnessed. Among these, the conical form of vortex breakdown is less explored in the literature. In this paper, much attention is therefore focused on exploring the governing mechanism of conical breakdown. It is should be interesting to note that, unlike other vortex breakdown modes, conical breakdown persists only for a very short band of S_G. For any small increase/decrease in S_G beyond a certain threshold, the flow spontaneously reverts back to the CTRZ state. Energy ranked and frequency-resolved/ranked robust structure identification methods – proper orthogonal decomposition (POD) and dynamic mode decomposition (DMD) respectively – are implemented over instantaneous time-resolved PIV data sets to extract the dynamics of the coherent structures associated with each vortex breakdown mode. The dominant structures obtained from POD analysis suggest the dominance of the Kelvin–Helmholtz (KH) instability (axial + azimuthal; accounts for $\sim$80 % of total turbulent kinetic energy, TKE) for both PVB and CTRZ while the remaining energy is contributed by shedding modes. On the other hand, shedding modes contribute the majority of the TKE in conical breakdown. The frequency signatures quantified from POD temporal modes and DMD analysis reveal the occurrence of multiple dominant frequencies in the range of $\sim$10–400 Hz with conical breakdown. This phenomenon may be a manifestation of high energy contribution by shedding eddies in the shear layer. Contrarily, with PVB and CTRZ, the dominant frequencies are observed in the range of $\sim$20–40 Hz only. We have provided a detailed exposition of the mechanism through which conical breakdown occurs. In addition, the current work explores the hysteresis (path dependence) phenomena of conical breakdown as functions of the

† Email address for correspondence: sbasu@iisc.ac.in

Reynolds and Rossby numbers. It has been observed that the conical mode is not reversible and highly dependent on the initial conditions.

---

1. Introduction

The fundamental understanding of vortex breakdown and jet interaction mechanisms in coaxial swirling flow is of high practical value in many engineering applications (Gupta, Lilley & Syred 1984). Vortex breakdown is a common feature in swirling flows, which will occur if the ratio of azimuthal to axial velocity exceeds certain threshold limit (Benjamin 1962; Hall 1972). The type and mechanism of vortex breakdown in swirling flows are usually characterized by a non-dimensional parameter named the swirl number (S), which theoretically represents the flux ratios between tangential and axial momentum. In general, swirl number $S \geqslant 0.6$ is interpreted as a strong swirling jet; the flow beyond this threshold is known to exhibit vortex breakdown (Benjamin 1967).

Insights into the evolution of swirling flows at various spatio-temporal scales is extremely important in modern-day gas turbine combustors to optimize the design (Lefebvre 1998), suppress combustion instability and enable robust flame holding. In these combustors, fuel is injected continuously either in the form of a liquid spray or gaseous jet in the highly turbulent coaxial swirling flow. The high momentum associated with coaxial swirling flow results in significant energy transfer to the injected fuel jet (Rajamanickam, Roy & Basu 2018) (also known as a secondary jet). During this momentum transfer process, the complex instability modes associated with swirl flows are also imposed over the secondary jets (Rajamanickam & Basu 2017a). The resultant jet–jet interaction mechanism is a key parameter in determining the spatio-temporal fluctuations in mixing, combustion efficiency and emission in combustors. Unlike coaxial round jets, in swirling flows, the presence/dominance of momentum in the azimuthal direction leads to a phenomenon called 'vortex breakdown'. It is well known that the persistence of vortex breakdown induces several complicated instabilities (helical, centrifugal shear etc.) in the flow field (Cassidy & Falvey 1970; Gallaire & Chomaz 2003a). Several experimental and numerical works have been carried out to precisely represent the forms of vortex breakdown in such flows (Harvey 1962; Spall, Gatski & Grosch 1987; Lopez 1990).

Although various types of vortex breakdown (single, double helical, axisymmetric bubble) have been reported, all exhibit a universal behaviour of stagnation point formation in the near field of the nozzle (Harvey 1962). Furthermore, this phenomenon gives rise to deceleration of injected flow which ultimately leads to flow reversal towards the burner exit. In addition, a special form of breakdown named the 'conical sheet' type breakdown is witnessed by Billant, Chomaz & Huerre (1998) and Santhosh, Miglani & Basu (2014) in their coaxial swirling jet experiments. Both authors have mentioned that the conical form of breakdown is highly unstable and appeared only over a very short range of swirl numbers. Billant *et al.* (1998) also showed the hysteresis associated with conical breakdown pathways.

Among all types of vortex breakdown, the bubble type is found to be more relevant in gas turbine combustors (Gupta *et al.* 1984; Escudier & Keller 1985; Lucca-Negro & O'doherty 2001). However, the bubble type of breakdown is accompanied by

the formation of a precessing vortex core (PVC) which ultimately induces helical disturbances in the flow (Loiseleux, Chomaz & Huerre 1998). Furthermore, PVC is known to greatly influence reactant mixing, flame propagation and ignition due to the time-varying nature of stagnation point in the near field (Stöhr, Arndt & Meier 2013, 2015). Wang *et al.* (2016) showed that helical breakdown can even appear in bubble type breakdown due to global three-dimensional instability. The theoretical analysis proposed by Chakraborty, Balachandar & Adrian (2005) and Meliga, Gallaire & Chomaz (2012) also reveals that the essential feature of bubble type vortex breakdown (VB) is manifested by the presence of helical structures. In addition, the counter-rotating vortices arising from bubble breakdown induces strong precessing of helical structures. This phenomenon results in the formation of three-dimensional complicated coherent structures (Cala *et al.* 2006).

The identification and quantification of the dynamics associated with such coherent structures induced by VB are of ceaseless interest in swirling flows. Most of the earlier investigations adopt flow visualization techniques to delineate the VB mechanisms in swirl flows. For instance, Sarpkaya (1974) and Faler & Leibovich (1977) employed dye based flow visualization methods to qualitatively understand the spatially evolving structures in swirl flows as manifested by different VB modes. Though flow visualization techniques qualitatively addressed the spatial structures as a function of swirl strength, they fail to predict the temporal dynamics of VB modes. In late 1990s, the development of laser diagnostic techniques enabled researchers to gain more insights into hydrodynamic instabilities. Among these, particle tracking/image velocimetry (PTV/PIV) received greater attention because of their planar measurement capabilities. The advent of data reduction techniques such as POD (proper orthogonal decomposition), DMD (dynamic mode decomposition) offered powerful tools towards extracting the relevant dynamical features of the flows.

Oberleithner *et al.* (2011) implemented POD techniques over instantaneous velocity fields to delineate energetic spatial structures. His results showed the occurrence of helical disturbances in the flow. Later, Markovich *et al.* (2014) employed POD and DMD methods to identify the dominant structures in weak and strong swirling flames in a combustor. Tilted helical and co-winding helical vortices are identified as dominant coherent structures in the weak and strong swirling jet respectively. In addition, their temporal analysis showed that the flow is highly dominated by global helical disturbances with a frequency of $\sim$233 Hz. Wilson, Mejia-Alvarez & Prestridge (2015) and Roy *et al.* (2017) have also attempted to use POD, DMD techniques to identify the mechanism likely to govern the flame dynamics in swirl flows. For instance, Roy *et al.* (2017) employed modal analysis on simultaneous time-resolved PIV/planar laser induced fluorescence (PLIF) data to identify the dynamics modes in highly turbulent swirling flames. Their analysis revealed a dominant PVC frequency around $\sim$800 Hz. Subsequently, the spatial modes pertaining to this frequency were identified as helical modes.

1.1. *Scope of the work*

The literature survey briefly discussed in the previous section clearly shows a lack of understanding of the dynamics of vortex breakdown in swirling flows. In particular, conical breakdown, which is considered to be a highly unstable state in coaxial swirling flows, has not been explored in great details. This conical breakdown mode is significant since in real life combustors it can affect adversely the flame holding capacity leading to sudden blowoff events. Particularly for aeropropulsion, such blowoff events can be catastrophic.

Although globally vortex breakdown has been analysed by several classical works (Benjamin 1962; Leibovich 1978; Billant *et al.* 1998; Gallaire & Chomaz 2003*b*), the underlying mechanisms which governing the temporal dynamics are still not clear. In this study, an attempt has been made to understand the dynamics of various forms of vortex breakdown in coaxial swirl flows using high fidelity time-resolved laser diagnostics. Furthermore, in most of the studies, experiments are performed either only with swirl jets or coaxial jets with fixed swirl number (such as vane swirlers). To address this research gap, in the present study, the experimental set-up is designed in such a way as to vary co-annular jet and swirl jet in an independent manner. This arrangement ensures that a much wider parameter space can be easily studied. Lastly, the mechanism of conical breakdown and the precursor events leading to such events have been explored rigorously across a large experimental space.

The present investigation shown in this paper is structured as follows.

In § 2, we explain the experimental configuration, details of the optical diagnostic tools and their arrangement. In addition, the flow conditions and non-dimensional numbers are also shown. The global evolution of the time-averaged flow as a function of various swirl numbers (S) for fixed co-annular Reynolds number is presented in § 3. This includes experiments carried out across y–r and multiple r–θ planes. Subsequently, § 4 describes the POD analysis performed to extract the dominant spatial and temporal modes. The dominant spatial structure pertaining to each flow condition is delineated as a percentage of turbulent kinetic energy. It enables us to interpret the possible governing mechanisms associated with each VB mode. In particular, we focus our attention on the analysis of conical breakdown. In § 4.2, we discuss the dominant unstable modes perceived from frequency ranked DMD analysis. Here, comparative interpretation between POD and DMD modes is also presented. Finally, the hysteresis associated with conical breakdown across various co-annular flow Reynolds numbers are discussed in greater details in § 4.4.

In our previous studies (Santhosh, Miglani & Basu 2013; Santhosh *et al.* 2014; Santhosh & Basu 2015), the global evolution of the resultant flow structure across various swirl numbers has been reported in great detail. However, being a low-speed measurement ($\sim$5 frames s^{-1}), the dynamics pertaining to each flow mode is not addressed rigorously. Whereas, in the present study time-resolved PIV ($\sim$1500 frames s^{-1}) enables us to delineate the various VB modes in a more insightful manner. For example, we are able to answer questions such as what causes the flow to undergo conical breakdown from the bubble mode along with the precursor events? In addition, experiments have been carried out at higher Reynolds numbers to evaluate the hysteresis associated with various VB modes.

2. Experimental conditions and procedure

The schematic of the swirl stabilized burner utilized in this study is shown in figure 1. The set-up consists of coaxial annular and tangential air passages. In this study, the swirl is imparted to the air flow with the help of tangential inlets provided at the burner exit. Here, an even number of tangential slots (a total of 8) has been used to ensure uniform distribution of swirling flow. Further information pertaining to the geometrical details of the burner can be found in Santhosh *et al.* (2013, 2014).

Air flow rate across all the passages has been metered using a thermal mass flow controller (make: M/s. Alicat, Inc). Two layers of honeycombs are placed in the co-annular pipe to condition the flow before it reaches the burner exit.
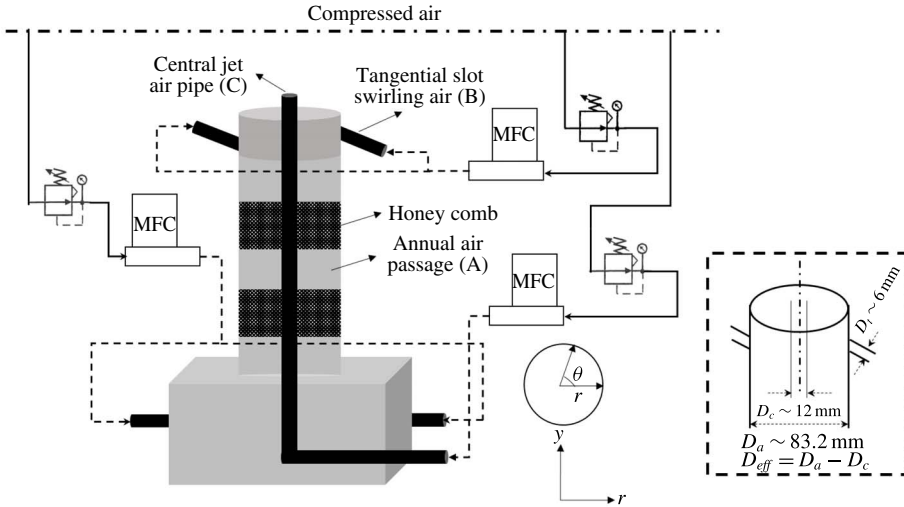
FIGURE 1. Schematic of experimental set-up.

2.1. *Measurement methodology*

Time-resolved PIV

It is well known that the inherent instabilities present in swirl flow lead to complex coherent structures. It is hence mandated to employ time-resolved measurements to understand the flow dynamics. In general, experimental techniques like hot-wire anemometry (HWA), laser Doppler velocimetry (LDV) are more powerful in terms of dynamic (temporal) response (usually $\sim$20–50 kHz). However, being point measurement techniques, their usages are limited to local measurements. Hence, planar measurements like PIV are usually preferred to resolve the large spatial scales. In this study, time-resolved PIV is employed to meticulously analyse the spatio-temporal characteristics of the swirling flow field.

A high repetition rate ($\sim$10 kHz; make: Photonics Inc.) dual pulsed Nd:YLF laser with a pulse energy of 30 mJ pulse^{-1} is used as an illumination source. The cylindrical beam of the laser output is converted into a thin sheet ($\sim$1 mm) using sheet making optics. This optics comprises two telescopic lenses and one cylindrical lens. The purpose of the telescopic lens is to adjust the beam diameter thereby the light sheet thickness. The aperture angle (α) of the sheet is controlled by the focal length (f) of the cylindrical lens. In this study, 'f' is chosen as 10 mm to ensure proper illumination of the required field of view.

The flow has been seeded with diethyl hexyl sebacate oil (DEHS) as tracer particles. The size of the particles is chosen as $\sim$1–3 μm to maintain better tracing accuracy (i.e. Stokes number, $St \ll 1$). The seeded flow is illuminated with the laser and the light scattered by the oil particles is recorded with a high-speed camera (make: Photonics Inc; 7000 frames s^{-1} at the full resolution of 1024 pixel $\times$ 1024 pixel). The laser pulse and camera shutter are synchronized using a programmable timing unit (PTU) to yield the time frozen snapshots. Furthermore, an optical bandpass filter of 527 nm is coupled with a camera lens to avoid noisy scattered signals from the ambient. The camera is operated in double frame mode with the optimal time delay 'dt' between two frames.
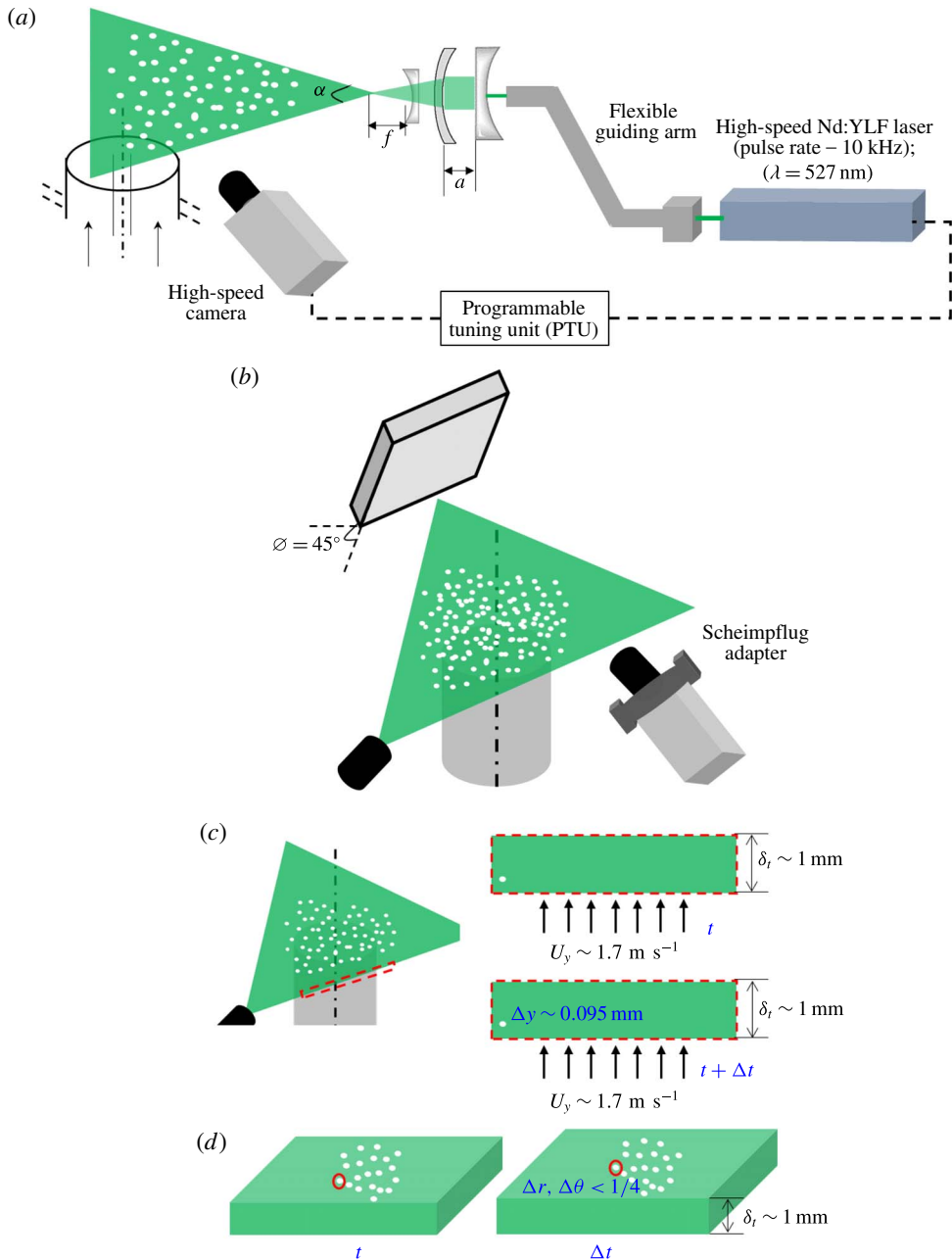
FIGURE 2. (Colour online) Schematic showing the optical arrangements of PIV system (*a*) *y*–*r* plane; (*b*) *r*–*θ* plane; (*c*) out of plane motion in an *r*–*θ* plane; (*d*) optimal displacement of particles across two frames in an *r*–*θ* plane.

In this study, PIV is done in the *y*–*r* as well as the *r*–*θ* plane. For *y*–*r* plane measurements the laser sheet is aligned with the longitudinal plane of the burner (see figure 2*a*). The laser sheet is flipped to horizontal orientation and aligned parallel to the burner exit (figure 2*b*). This facilitates measurements at different *y/d* locations. In

both cases, the camera is positioned orthogonal to the plane of illumination. During r–θ measurements, the plane of illumination is projected towards the overhead mirror which is oriented at $\sim$45° with respect to the vertical stand (see figure 2*b*). A Scheimpflug adapter is coupled to the camera lens to enable fine adjustment between the image and lens planes without altering the camera position. Since the camera is viewing the plane in an oblique manner, it is necessary to correct for angular distortion. This is accomplished by employing a calibration plate with predefined spatial dots. The Scheimpflug adapter is finely adjusted to make sure all the dots in the calibration plate are clearly visible. It is common practice to select 'dt' (pulse separation time in PIV) in such a way that the spatial displacement of the particle across the two frames should be less than 1/4 of the interrogation window (IW) size. To evaluate the optimal 'dt', experiments are started with zero displacement (i.e. a very low value say, $\sim$6 µs), then dt is slowly increased till $\leqslant$1/4 IW. In the present study, the final IW size is chosen to be 32 pixel $\times$ 32 pixel for both r–θ and y–r planes.

In particular, 'dt' is chosen with special care for r–θ measurements, to ensure the detection of the same particle in the second frame since the strong axial velocity can lead to out of plane motion of the particles.

For instance, with $Re_a \sim 4896$ case, the maximum axial velocity (U_y) at the burner exit is found to be 1.7 m s^{-1}. The maximum axial displacement of the particle for the chosen 'dt' (i.e. 95 µs) is found to be $\sim$0.095 mm (figure 2*c*), which is much less than the laser sheet thickness $\sim$1 mm. The corresponding values for $Re_a \sim 10\,545$, 17 456 are found to be 0.11 mm, 0.19 mm respectively (all <1 mm). In addition, the selected 'dt' also satisfies the optimal displacement criteria (i.e. Δr, $\Delta \theta < (1/4)IW$; $\sim$5 pixel; figure 2*d*). The values of 'dt' in the r–θ plane for $Re_a \sim 4896$, 10 545, 17 546 are chosen as 95 µs, 50 µs, 25 µs respectively.

The same optimal pixel displacement criteria have been also extended to y–r plane too (i.e. Δr, $\Delta y < (1/4)IW$). In the y–r plane, the optimal 'dt' for $Re_a \sim 4896$, 10 545, 17 546 are chosen as 105 µs, 77 µs, 40 µs respectively.

Furthermore, the accuracy of the flow field perceived from PIV is greatly influenced by laser sheet thickness (δ_t), particle displacement across two frames (ds) and number of particles (N) per IW. The correctness of the above-mentioned parameters is validated by employing 'correlation statistics' method (Sciacchitano, Wieneke & Scarano 2013; Wieneke 2015). This method attempts to evaluate the uncertainty in the measured velocity values (u_{error}) based on the positional disparity between the correlation peaks observed across the two frames. In the present study, the uncertainty in the measured velocity values is found to be $\sim \pm 1.3\%$ (r–θ) and 1% (y–r plane) of the local velocity values. More technical operational details involved in PIV like optimal seeding density, dt, laser sheet thickness can found in Raffel *et al.* (2013).

Further, we acknowledge that stereoscopic (three-dimensional) high-speed PIV may bring additional insights into the flow dynamics (especially in the r–θ plane). The three-dimensional (3-D) vector field can be confidently calculated only in the overlapped region of cameras 1 and 2 (Arroyo & Greated 1991; Prasad & Adrian 1993) using stereo or tomographic PIV. In the present work, the flow spread area is much higher (especially with conical breakdown) than the overlap area one can expect in stereo mode. Hence, we have not attempted stereoscopic PIV in this study due to equipment limitations. At the same time, the acquisition of all three component of velocities (U_r, U_y, U_θ) in simultaneous fashion improves the understanding of the problem. Since, the swirling flow is known to be highly three-dimensional flow, 3-D measurements may help to delineate the vortex breakdown mechanisms

in a more insightful manner. In the present work, all three components of velocity have been acquired, but not in the same temporal space. In addition, 2-D PIV also ignores particles with strong out of plane motion leading to errors. The absence of tomographic PIV data is therefore considered a limitation in the present study. However, the same will be taken up in our future work. However, we have tried to keep the errors incurred due to 2-D PIV to a minimum (as explained previously).

Throughout the experiments, images are acquired at 1500 frames s^{-1} with an acquisition time of 2 s (i.e. 3000 images are considered per each test case). For most of the y–r measurements, the field of view (FOV) is chosen as 140 mm $\times$ 140 mm with a spatial resolution of $\sim$7.2 pixels mm^{-1}. During r–θ measurements, the same is kept at $\sim$280 mm $\times$ 280 mm ($\sim$3.65 pixels mm^{-1}). It should be noted that for most of the near-field measurements ($y/R_a \leqslant 0.5$), smaller field of view ($\sim$180 mm $\times$ 180 mm) is adapted to yield a high spatial resolution of $\sim$5.68 pixels mm^{-1}.

The acquired double frame PIV raw images are post-processed using Lavision 8.4 software to reconstruct the vector fields. For all the test cases, multipass interrogation windows (IW) with decreasing sizes are employed with initial and final window sizing being 48 pixel $\times$ 48 pixel and 32 pixel $\times$ 32 pixel respectively. In addition to this, adaptive PIV option is employed to enable auto calculation of window shape based on the gradient in the flow field.

2.2. *Planar laser Mie scattering experiments (PLMS)*

In addition to PIV measurements, a Nikon D7200 DSLR camera is used to perform a planar laser Mie scattering experiment. This experiment provides qualitative visualization of flow topologies at the burner exit across various operating conditions. Here, the optical arrangements are similar to the y–r plane PIV measurements, except that the camera is operated in video grabbing mode. The flow is seeded with the same DEHS oil; the light scattered by the oil particles from the illuminated plane is recorded with the DSLR camera. It is important to note that a higher seeding density is employed to generate smoke-like flow visualization images. PLMS experiments are carried out only in the y–r plane. Two macro lenses, 100 mm (make: Tokino) and 50 mm (make: Nikon), are used to image the near field and far field of the flow. With both lenses, videos are recorded at 30 f.p.s. (full HD 1080 p).

2.3. *Flow conditions*

The present study involves air flow across three different passages (A, B, C; see figure 1), hence it is necessary to define non-dimensional numbers to identify the parametric relationships among the different flow configurations. The experiment has been carried out at three sets of flow rates across annular (A) and central pipe (C) passages. At each set, the flow rate across tangential entry (B) is progressively varied to impart a different level of swirl intensity to the annular flow. The experimental test cases are globally characterized using three important non-dimensional numbers namely, the Reynolds number, momentum ratio and swirl number.

Reynolds number (Re) can be defined as

$$Re_g = \frac{\rho_a U_o D_{eff}}{\mu_a}, \tag{2.1}$$

where, ρ_a, μ_a are air density (kg m^{-3}) and viscosity (Pa s), D_{eff} is effective burner diameter (m); U_o is bulk-averaged velocity of the fluid at burner exit (m s^{-1}):

$$U_o \sim \frac{A_c U_c + A_a U_a + A_t U_t}{A_c + A_a + A_t}. \tag{2.2}$$

Here, A_c, A_a, A_t are cross-sectional areas available for the central, annular and swirl jet, respectively. U_c, U_a, U_t are corresponding bulk average velocities computed based on the volumetric flow rate. Hence it should be noted that Re_g is basically a bulk-averaged flow Reynolds number at the burner exit.

Further, only the annular flow (i.e. flow across A and B) Reynolds number (Re_a) is defined by neglecting the A_t, U_t terms in the expression (2.2).

In coaxial jets, it is customary to define the momentum ratio (MR) as a quick estimate to quantitatively understand the momentum transfer pathways among coaxial jets. In general, the jet whose flow rate is variable is defined in the numerator part and the jet with constant air flow rate is kept in the denominator. Since, in this study, for the given co-annular flow across A and C, the flow rate across the tangential port is progressively varied, the MR can be defined as follows,

$$MR = \frac{\rho_a U_t^2}{(\rho_a U_a^2 + \rho_c U_c^2)}. \tag{2.3}$$

In single phase coaxial jets, since the density is same for all of the fluids, equation (2.3) becomes the velocity ratio

$$MR = \frac{U_t^2}{(U_a^2 + U_c^2)}. \tag{2.4}$$

Swirl number is quantified as a function of the axial flux of tangential momentum and axial flux of axial momentum:

$$S = \frac{\int_{R_h}^{R_o} \rho U_y U_w 2\pi r^2 \, dr}{\int_{R_h}^{R_o} \rho U_y^2 2\pi r \, dr}. \tag{2.5}$$

However, Claypole & Syred (1981) showed that the swirl number can be defined in terms of the burner geometry (2.6)

$$S_G = \frac{\pi r_o r_a}{A_t} \left\{ \frac{m_t}{m_a + m_c} \right\}^2, \tag{2.6}$$

where, r_o is the radial distance between the burner central axis and the tangential port, r_a is the inner radius of the annular pipe (A), m_a, m_c, m_t are respectively the annular, central, tangential flow rates (in l min^{-1}). In common practice, geometric swirl number S_G is related to S in terms of $S \sim 0.25 S_G$.

In addition to the MR and the swirl number, the influence of inlet flow conditions on the final flow field structure can be delineated by a parameter named the Rossby number,

$$Ro \sim |\Delta U_y|/U_t, \tag{2.7}$$

Test cases	Annular flow Reynolds number (Re_a)	Tangential air flow rate (1 min^{-1})	Bulk-averaged Reynolds number (Re_o)	Momentum ratio (MR)	Swirl number (S_G)	Modes of vortex breakdown
A1		0	4896	0	0	—
A2		30	4958	0.20	0.58	—
A3		100	5047	7.50	1.76	PVB
A4	4896	120	5083	10.79	2.28	CTRZ
A5		125	5092	11.72	2.40	Transition
A6		130	5100	12.68	2.53	CB
A7		135	5108	13.67	2.67	Transition to CTRZ
A8		140	5118	14.70	2.80	CTRZ
B1		0	10 545	0	0	—
B2		100	10 665	0.94	0.55	—
B3		150	10 754	5.42	1.66	PVB
B4	10 545	200	10 844	9.64	2.28	CTRZ
B5		250	10 933	15.06	2.47	Transition
B6		280	10 986	18.89	2.55	CB
B7		300	11 022	21.69	2.92	CTRZ
C1		0	17 456	0	0	—
C2		200	17 782	0.98	0.79	—
C3		300	17 985	3.30	1.50	PVB
C4	17 546	400	18 163	5.9	2.27	CTRZ
C5		420	18 217	6.78	2.43	Transition
C6		440	18 270	7.77	2.57	CB
C7		500	18 448	11.51	3.06	CTRZ

TABLE 1. Experimental test cases. PVB – pre-vortex breakdown; CB – conical breakdown; CTRZ – central toroidal recirculation zone.

where,

$$\Delta U_y \sim U_c - U_a. \tag{2.8}$$

Here, U_c, U_a indicates the bulk average exit velocities, which are calculated based on the flow rate and exit diameter of the annular and central pipes, respectively.

Theoretically, the Rossby number (Ro) represents the ratio of axial and radial pressure gradient. In swirling flows, it is well known that flow with a dominant radial pressure gradient undergoes vortex breakdown.

The experimental test cases are listed in table 1, it should be noted that the experimental runs are not only confined to the values shown here. For instance, while flow undergoing a transition from CTRZ to conical breakdown (CB) (figure 3), experiments are carried out for small variations in tangential mass flow rate ($\Delta m_t \sim$ 3–5 1 min^{-1}) to carefully identify the flow/vortex breakdown modes. The importance of employing small Δm_t will be elucidated in greater detail in subsequent sections.

The main aim of this study is to elucidate the effect of swirl intensity on annular flows, in particular, for a given Re_a, how the flow topologies vary with swirl number S_G. During this process, it is observed that the flow undergoes different forms of topological variations (like PVB, CB, CTRZ etc. figure 3).
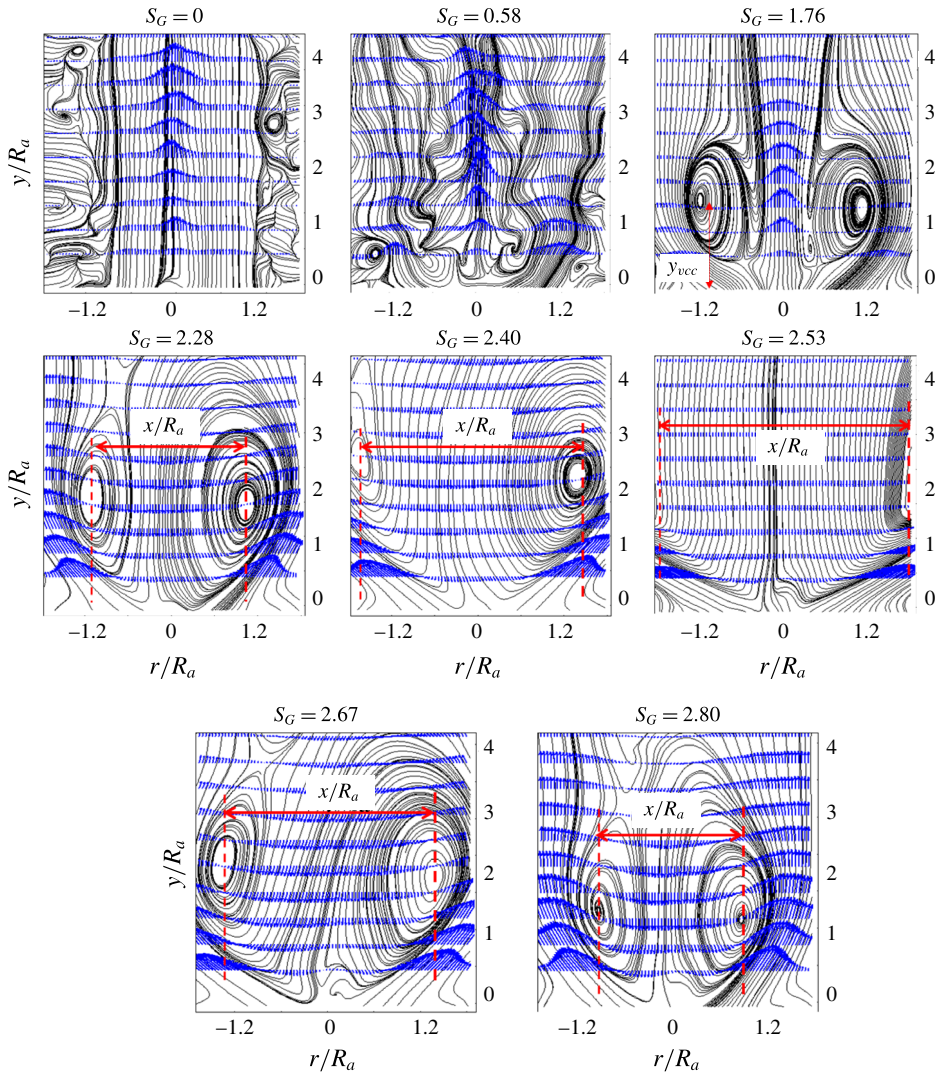
FIGURE 3. (Colour online) Time-averaged vector field superimposed with streamlines (A1–A8).

3. Global observations

This section outlines the global evolution of the flow field as a function of swirl number (S_G) for given (Re_a). The time-averaged flow field acquired from time-resolved PIV measurements, for $Re_a = 4896$ across different S_G values are shown in figure 3. The time-averaged flow field is an average of 3000 instantaneous flow field images (i.e. 2 s of temporal data).

Here, the flow field pertaining to one complete cycle (i.e. non-vortex breakdown to CTRZ) of flow transitions is considered. The vector field shows dominant behaviour in the axial direction for non/weak swirling jets ($0 \leqslant S_G \leqslant 0.58$); this is due to the weak momentum ($MR < 1$) of the swirl jet compared to the annular jets. In the present study, for $0 \leqslant S_G \leqslant 0.58$, the value of Ro is found to be greater than 1, which
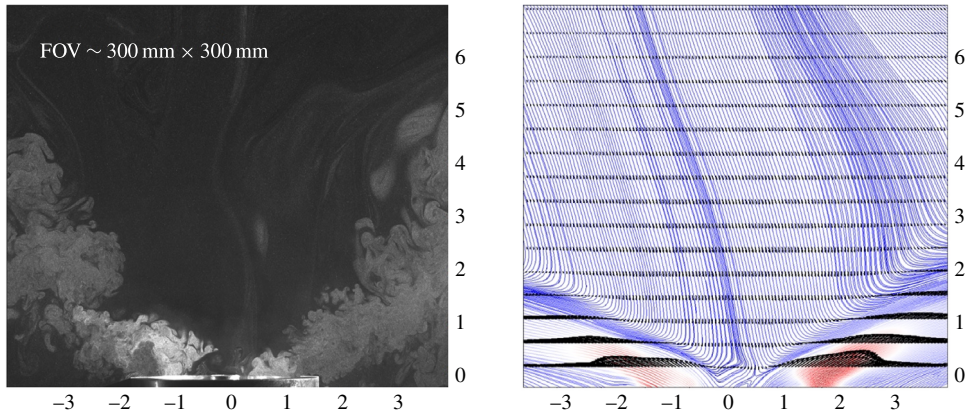
FIGURE 4. (Colour online) Illustration of time-averaged flow field of conical breakdown at $Re_a \sim 4896$ acquired with a wide field of view lens.

signifies dominance of the axial velocity component and resistance towards the vortex breakdown phenomenon. Further increase in swirl number leads to dominance of the centrifugal force and favours vortex breakdown and conical breakdown (figures 3 and 4). Although the signature of the vortex breakdown i.e. counter-rotating eddies is observed at $S_G \sim 1.76$, the presence of an axial central jet (C) prevents the formation of a recirculation zone. Hence, this state is named pre-vortex breakdown ($Ro \geqslant 1$). Furthermore, as evident from the time-averaged flow field observed in the r–θ plane, the radial expansion of the flow in the PVB case is constrained by the dominance of the axial jets (figure 5; $S_G \sim 1.76$). Beyond this point ($S_G \geqslant 2.28$), the increased centrifugal momentum/pressure gradient ($\sim \rho U_t^2$) induced by swirl flow causes a pressure deficit along the jet axis, which ultimately results in the formation of a recirculation zone. The flow transition from PVB to CTRZ state is delineated as the first transition point and the corresponding flow conditions are marked as critical parameters, namely $(Re_o)_{c1}$, MR_{c1}, $(S_G)_{c1}$. Beyond the transition condition ($MR \geqslant MR_{c1}$), the central jet is completely entrained by the coaxial swirl flow with radially outward expansion (see figures 3 and 5; $S_G \sim 2.28$). At this point, the flow exhibits shear layer instability in the axial as well as azimuthal direction.

The radial expansion of the flow field while undergoing a transition from the PVB to CTRZ state can be visualized in supplementary movie 2 available online at https://doi.org/10.1017/jfm.2018.549. The special form of vortex breakdown named 'conical breakdown' is witnessed for a further increase in swirl number from the CTRZ case. However, it should be noted that the CB state persists for a very short range of S_G values (see movie 1). To precisely locate the conical breakdown state and elucidate the possible fluid dynamic routes, tests have been carried out for many flow conditions near the CB state (with an interval of $\Delta m_t \sim 3$–5 l min^{-1}). Furthermore, the flow conditions pertaining to CB is delineated as the second transition state ($(Re_o)_{c2}$, MR_{c2}, $(S_G)_{c2}$).

The detailed dynamics governing the formation of conical breakdown from the CTRZ mode will be elucidated in greater detail using the POD and DMD methods in later sections. In this section, only global observations made during the CB state are outlined. Two length scales namely, the distance between the vortex core centre of two counter-rotating eddies (x/R_a) and the distance between the vortex core centre
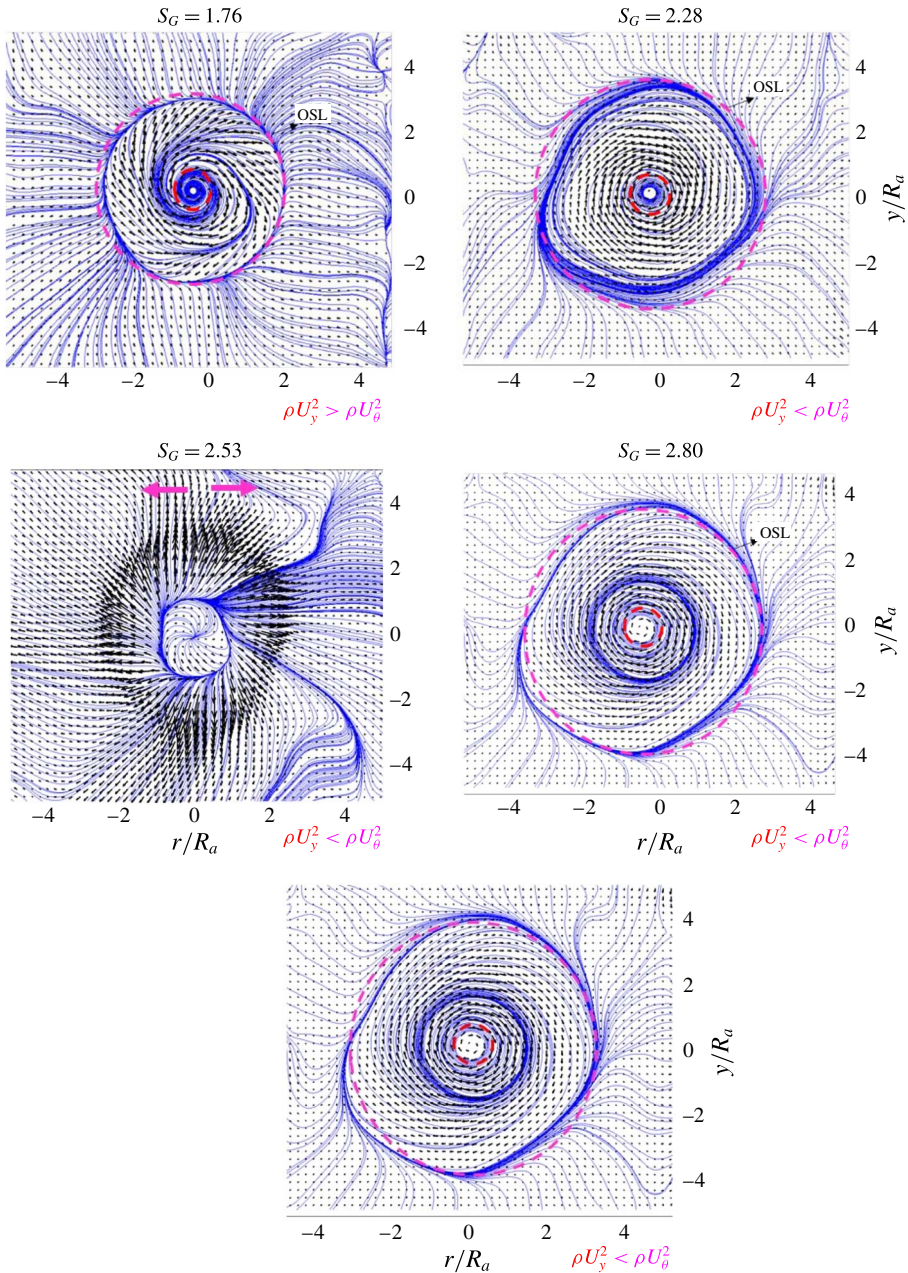
$$\rho U_y^2 > \rho U_\theta^2$$

$$\rho U_y^2 < \rho U_\theta^2$$

$$\rho U_y^2 < \rho U_\theta^2$$

$$\rho U_y^2 < \rho U_\theta^2$$

$$\rho U_y^2 < \rho U_\theta^2$$

FIGURE 5. (Colour online) Time-averaged flow field in an r–θ plane at $y/Ra = 0.3$. ($Re_a \sim 4896$) (OSL – outer shear layer).

and the burner exit (Y_{vcc}/R_a) have been employed. From the time-averaged flow field depicted in figure 3, it is clear that both length scales show an increasing trend on approaching the CB state. For instance, while S_G increases from 2.28 to 2.40, significant fanning of the recirculation zone is observed. In addition, the vortex core centre (Y_{vcc}/R_a) shifts upstream. Comparatively, the magnitude of Y_{vcc}/R_a for

pre-CB ($S_G \sim 2.4$) is slightly larger than that of post-CB ($S_G \sim 2.67$). Similar pattern is also reported by Billant *et al.* (1998). In the conical breakdown state (figure 3; $S_G \sim 2.53$), the counter-rotating eddies do not exist with the flow completely fanning out in the radial direction (see figure 5; $S_G \sim 2.53$). To cross-check the existence of counter-rotating vortices in CB, experiments have also been conducted in a large field of view ($\sim$300 mm $\times$ 300 mm) with the help of a 50 mm macro lens. However, counter-rotating vortices are not witnessed even with the large field of view (see figure 4).

The flow topology persists in the CB state only over a small range of swirl numbers ($2.53 \leqslant S_G < 2.67$), i.e. it recovers back to the CTRZ state. The process of flow undergoing transition to the CB from the CTRZ mode and its recovery back to the CTRZ state can be visualized in movie 1 (acquired with the DSLR camera from the planar Mie scattering experiment). The flow recovery from the CB to CTRZ state is marked as the third critical point and demarcated as $(Re_o)_{c3}$, MR_{c3}, $(S_G)_{c3}$. Furthermore, the CTRZ states attained before and after the CB mode are referred to as pre- and post-CTRZ.

In general, swirling flow always exhibits a certain degree of asymmetry (even for a time-averaged flow field) as a manifestation of strong PVC at higher swirling intensities (Syred 2006; Steinberg *et al.* 2012; Chterev *et al.* 2017). Lieuwen (2012) clearly delineated how the asymmetries are induced in the swirling flow as a consequence of strong PVC. He also showed that it is the formation of helical waves, in addition to axial and azimuthal KH waves, which essentially drive asymmetry in the flow field. Computational studies carried out by Huang, Wang & Yang (2005) in the coaxial swirl injector also delineate the same feature. Markovich *et al.* (2016) showed the occurrence of an asymmetric flow structure (at higher swirl number) from the high-speed tomographic PIV ($\sim$2 kHz) results. In addition, their three-dimensional flow field precisely showed how the evolution of the inner and outer helical vortices (IHV, OHV) leads to asymmetric structures.

The phenomenon of conical breakdown is reported only by a very few researchers (Sarpkaya 1971*a*; Billant *et al.* 1998). Lack of results and inherent technical complexities associated with CB leads to a poor understanding of the problem. For a coaxial flow, it is mandatory to identify the flow parameters which govern the conical breakdown. The above global observations as a function of flow parameters are schematically illustrated in figure 6.

Here, flow conditions are globally divided into two regimes namely the tangential (II) and axial momentum (I) dominated regions. It is seen that the Rossby number for the flow conditions pertaining to conical breakdown is always found be <1. In the conical breakdown state, any increase in flow which favours $Ro > 1$ results in the disappearance of the CB state. This observation clearly indicates that conical breakdown occurs only when centrifugal momentum is dominant over axial momentum (i.e. $\rho U_\theta^2 > \rho U_y^2$; $Ro < 1$). The time-averaged flow field corresponding to higher Reynolds numbers $Re_a \sim 10\,545$, $17\,456$ (i.e. B1–B7 and C1–C7) exhibits similar flow structures, as shown in figures 3 and 5. This may be due to the same swirl number value across all three Re_a values. This phenomenon has been observed by several researchers, for instance, Fu *et al.* (2007) and Rajamanickam & Basu (2017*b*). Hence, for brevity the flow field only pertaining to $Re_a \sim 4896$ is shown in this section.

Furthermore, it should be noted that, although the time-averaged topologies of the flow field are similar for the other Re_a values, the dynamic behaviour is very different at higher Reynolds numbers (particularly $Re_a \sim 17\,000$). For instance, at low flow
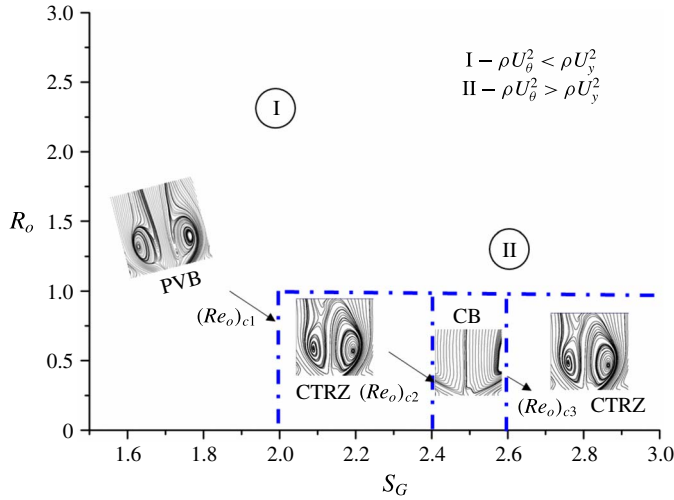
FIGURE 6. (Colour online) Global flow regime map.

rates ($Re_a \sim 4896$), the occurrence of conical breakdown (CB) is evidenced in both forward and backward pathways at the same air flow rates. However, the repeatability in the occurrence of CB does not follow the same path at the high air flow rates corresponding to $Re_a \sim 17\,000$. The same will be explained in greater detail using POD and DMD analysis in forthcoming sections.

More detailed information concerning the global flow topologies (vorticity maps, TKE distribution) as functions of swirl number can be found in our previous work (Santhosh *et al.* 2013, 2014).

3.1. *Evolution of shear layers in the flow field*

The evolution of shear layer in the spatial domain of the flow field across the different flow modes is illustrated in figure 7. It is seen that multiple shear layers exist for flows which exhibit vortex breakdown (see figure 7*b–e*). The PVB flow mode (figure 7*b*) exhibits two inner shear layers (ISL 1, ISL 2) and one outer shear layer (OSL 1). This is due to the combined dominance of the axial and centrifugal momentum induced by co-annular and swirling jets. During the CTRZ mode, ISL 2 completely vanishes due to the resistance offered by the recirculated flow against the axial jet. However, as the flow approaches the CB from the CTRZ mode, the ISL starts to shift towards the radial direction and its extent in the axial direction is also significantly reduced. Furthermore, with the full open cone configuration, the ISL almost vanishes and persists only in the near burner exit zone. The shear layers observed from the $r–\theta$ measurements across various S_G values are delineated in figure 5. Except for the CB case, the presence of the outer shear layer for all other flow modes is clearly witnessed. The outer shear layer does exist for the CB case, but it is far away from the burner central axis.

It should be noted that, excepting swirl number, parameters such as the momentum ratio (MR) and Rossby number (R_o) have been used to classify the flow into two paradigms i.e. in the given coaxial jet, whether the tangential flow is dominant ($U_\theta > U_y$ – regime II) or the axial jets are dominant ($U_\theta < U_y$ – regime I). Furthermore, as discussed in the above section, the flow modes are distinguished into three distinct types, PVB, CTRZ, CB as a function of S_G.
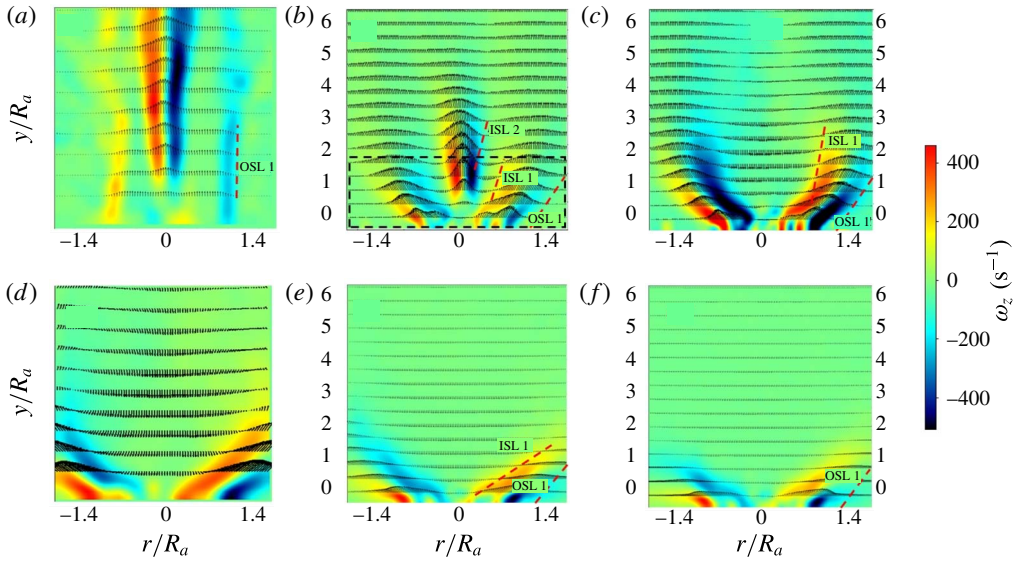
FIGURE 7. (Colour online) Evolution of shear layers across various S_G values. (*a*) $S_G \sim 0$; (*b*) $S_G \sim 1.78$; (*c*) $S_G \sim 2.28$; (*d*) $S_G \sim 2.4$; (*e*) $S_G \sim 2.5$; (*f*) $S_G \sim 2.53$ (OSL, ISL – outer, inner shear layer).

Hence, to avoid the confusion, instead of using all the non-dimensional numbers, thereafter only the flow modes (PVB, CTRZ, CB) and the corresponding swirl numbers are widely used in the forthcoming sections.

4. Vortex breakdown dynamics

The global observations presented in § 2 yield information on how the flow topology evolved as a function of the various swirl numbers. The results presented opened up several important questions. It is seen that conical breakdown occurs while the centrifugal pressure gradient is dominant. However, it is unclear why it persists only over a small range and recovers back to the CTRZ mode, although the flow is still centrifugally dominant. To understand this phenomenon, we have employed proper orthogonal and dynamic mode decomposition (POD, DMD) methods to identify dominant structures across different flow modes (PVB, CTRZ, CB).

4.1. *Proper orthogonal decomposition*

The essential role of the POD is to extract the most energetic structures from instantaneous flow field data. Additionally, POD enables us to quantify characteristic frequencies of the dominant modes from the temporal spectrum. In this study, we have implemented the 'method of snapshots' based POD algorithm (Sirovich 1987; Berkooz, Holmes & Lumley 1993) to decompose the flow field. The steps involved in the implementation of POD for given flow field data is shown in figure 8. Mathematically, this algorithm decomposes the instantaneous flow field data (U', V') into corresponding spatial $\emptyset_n(x)$ and temporal (j) modes. Further details on POD implementation for PIV data can be found in Rajamanickam & Basu (2017*b*).
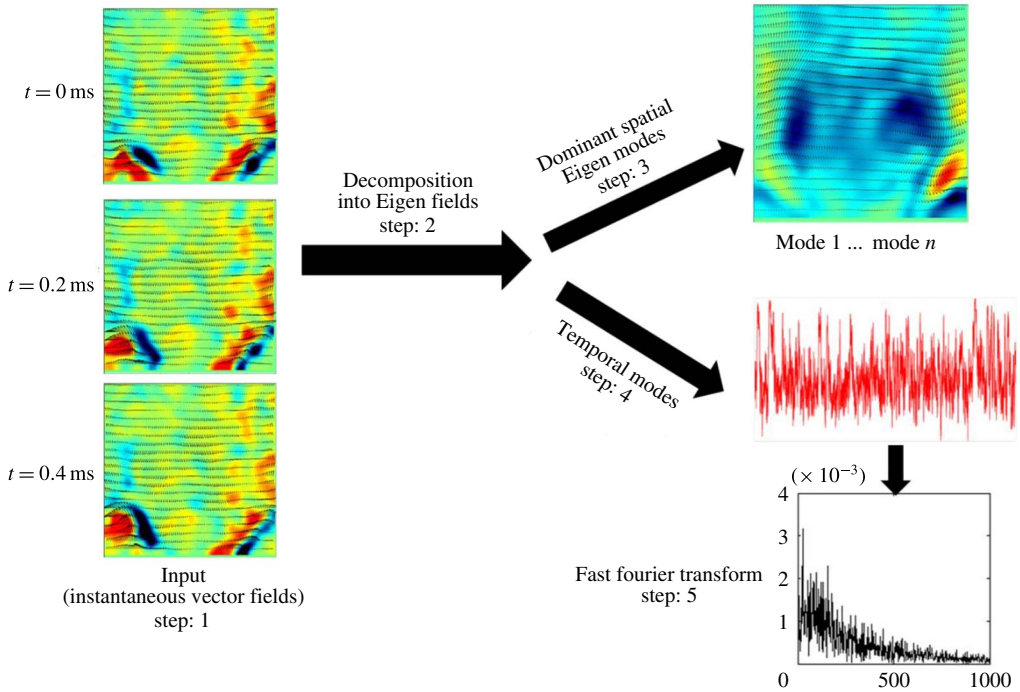
FIGURE 8. (Colour online) Steps involved in computing POD from the instantaneous flow field. Adapted from Rajamanickam & Basu (2017*b*).

4.1.1. *Temporal dynamics and spatial eigenmodes in the y–r and r–θ planes*

In general, the snapshot algorithm yields a spatial eigenmode number that equals the number of instantaneous data sets. However, the resultant eigenmodes are numbered in descending order of turbulent kinetic energy (TKE) magnitude (λ_n). For brevity, POD is carried out for those flow conditions which exhibit the vortex breakdown phenomenon (i.e. only for PVB, CTRZ, CB; $S_G \geqslant 1.76$). Additionally, POD analysis has been extended to the *r–θ* plane to meticulously understand the dynamics of vortex breakdown across different flow modes.

POD analysis has been carried out at many locations (*r–θ* planes), although the results pertaining to only three axial locations are explicitly considered. These three positions are considered such that key locations such as downstream and upstream of the VCC (see figure 10*a*) are covered. It is well known that frequency signatures perceived from fast Fourier transform (FFT) implemented over temporal modes yield more quantitative information on nature of the flow. Hence, for brevity, spatial eigenmodes are shown only for near-field locations ($y/R_a \sim 0.3$) and temporal modes are shown for all the defined locations.

Dynamics of pre-vortex breakdown (PVB)

The POD spatial eigenmodes pertaining to PVB, CTRZ, CB of the *y–r* plane are respectively shown in figure 9. Here vorticity maps are used to delineate the energetic modes. Since the cumulative energy of the first few modes contribute 90 % of the total energy, only those spatial modes are shown. In the PVB case, the most energetic mode (figure 9*a*, M1) clearly shows the dominance of axial shear induced by KH vortices of the co-annular jets at ISL 2. PVB case exhibits strong counter-rotating
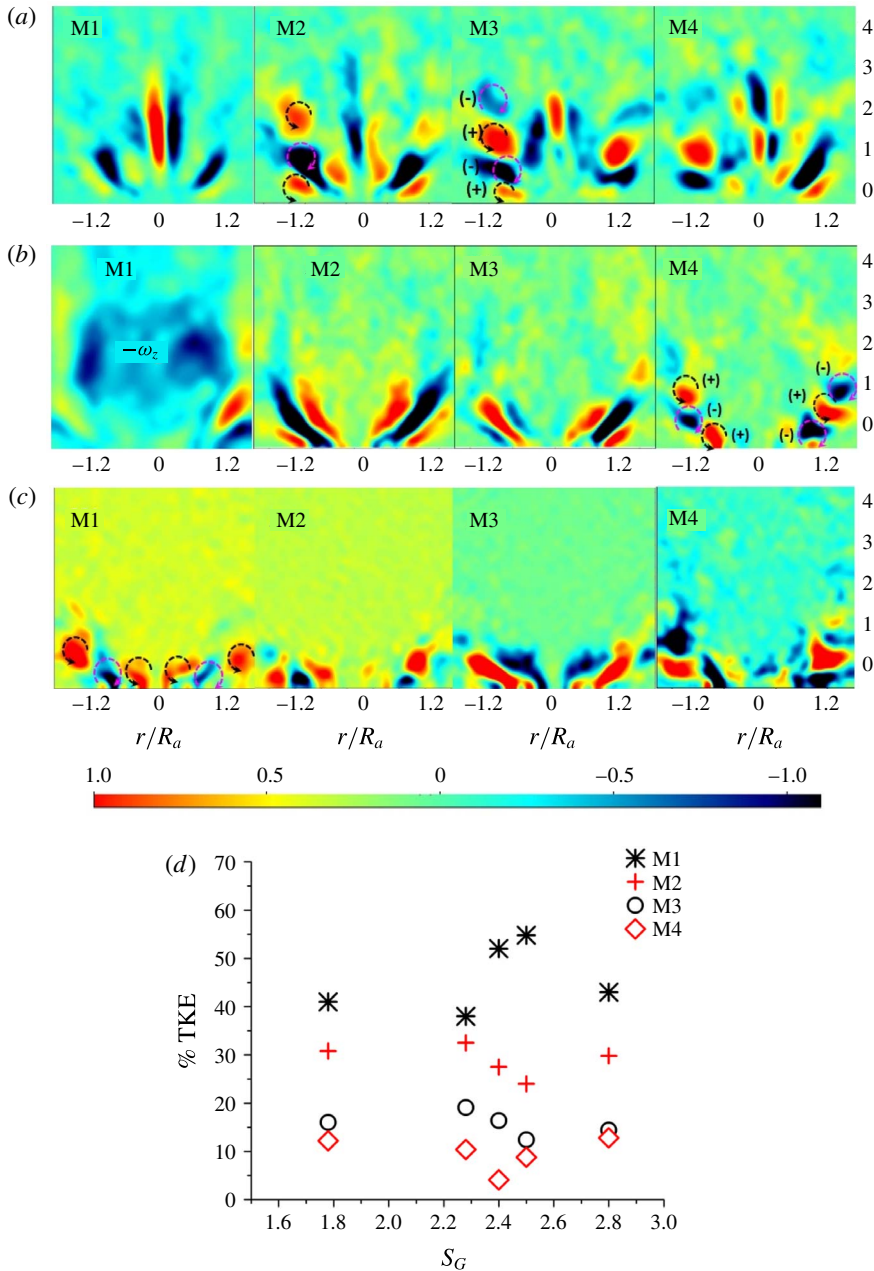
FIGURE 9. (Colour online) Illustration of spatial eigenmodes perceived from POD analysis in y–r plane at $Re_a \sim 4896$. (*a*) $S_G \sim 1.78 -$ PVB; (*b*) $S_G \sim 2.28 -$ CTRZ; (*c*) $S_G \sim 2.53 -$ CB; (*d*) distribution of % TKE across various POD spatial modes.

eddies in the near field of the burner (see figure 3 $S_G \sim 1.76$), leading to vortex shedding in the outer shear layer (OSL 1). This phenomenon is not intensified in mode 1, whereas, the same is clearly visible in modes 2–4 (figure 9*a*). More quantitative information on this observation can be perceived from the frequency signatures derived
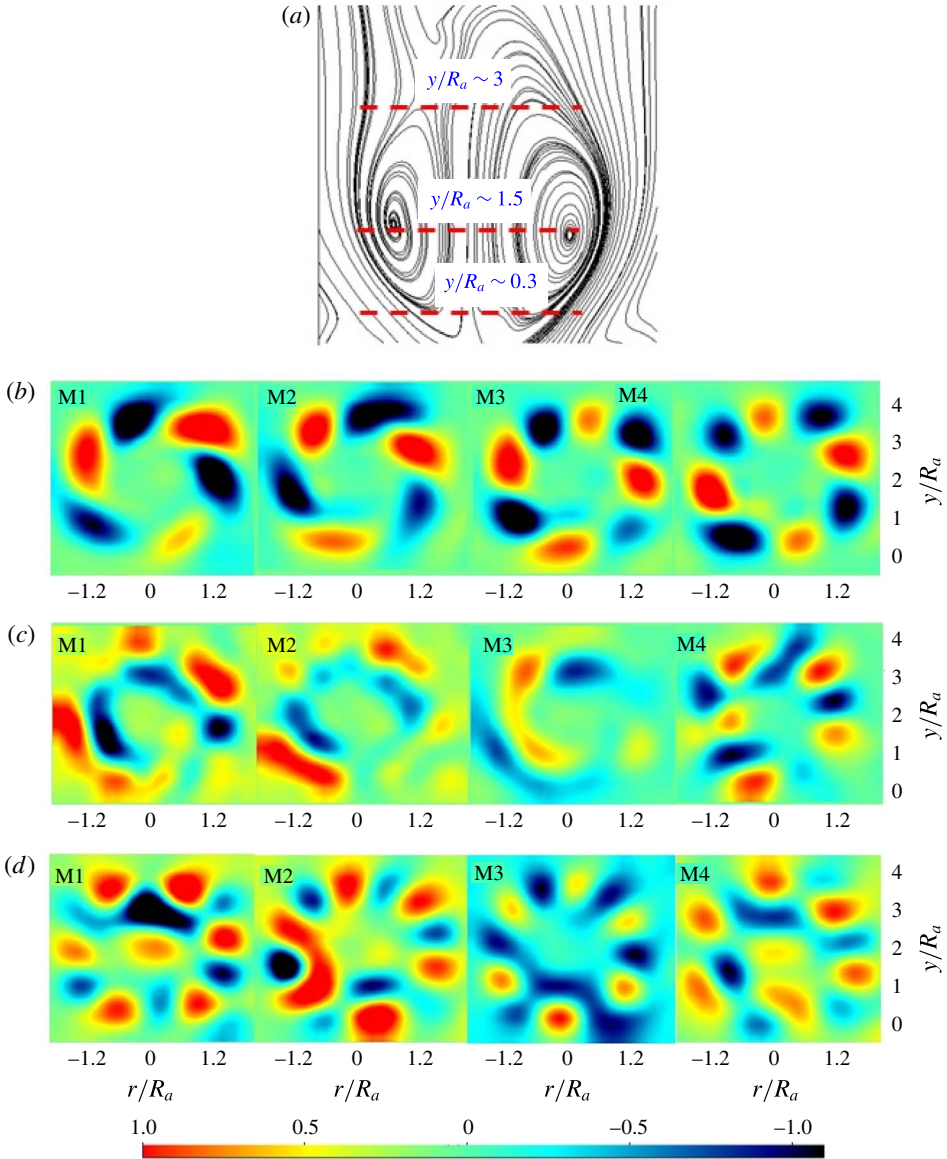
FIGURE 10. (Colour online) (*a*) Schematic illustration of spatial locations where POD analysis is carried out in an *r*–*θ* plane; (*b*–*d*) spatial eigenmodes of PVB, CTRZ, CB in near-field locations at $Re_a \sim 4896$ ($y/R_a \sim 0.3$).

from the POD temporal modes. In general, it is known that shedding eddies in the flow lead to frequency harmonics. From figure 11(*a*), it is evident that modes 2–4 show the existence of harmonics in the frequency signatures. On the other hand, mode 1 shows one strong peak around ∼20 Hz followed by higher-order frequencies with very small magnitude (this is due to the absence of shedding in mode 1; figure 9*a* M1). Furthermore, the instantaneous flow field suggests that the activation of shedding mode in the PVB case may be due to unsteadiness induced by the interaction of the swirling
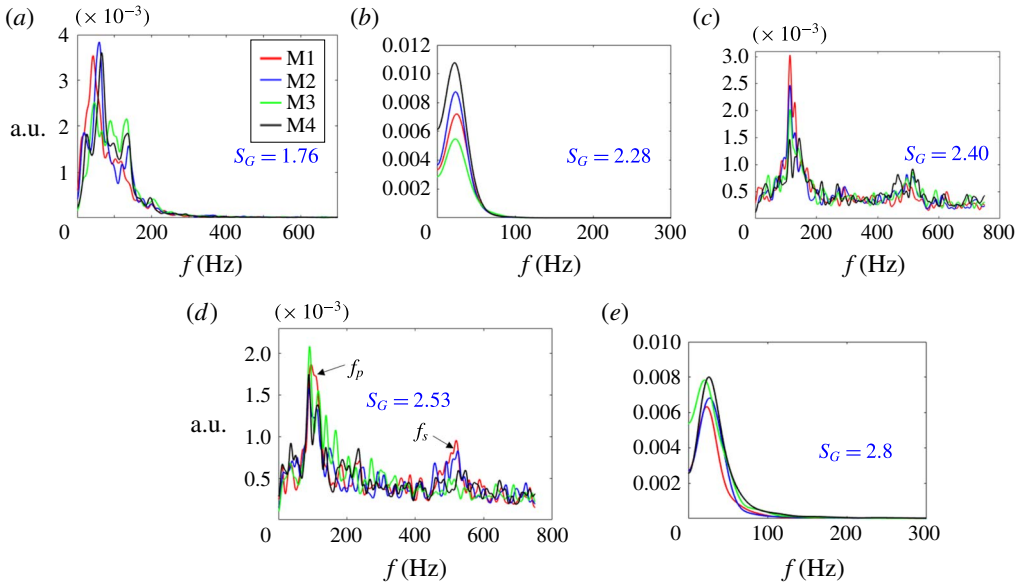
FIGURE 11. (Colour online) Schematic illustration of frequency signatures perceived from POD temporal modes in y–r plane across various S_G values. ($Re_a \sim 4896$.)

and co-annular jets in the near field. This can be interpreted in a quantitative manner from the POD analysis implemented over the r–θ plane.

As mentioned earlier, the activation of shedding modes in the PVB case is more pronounced in the near field (figure 12a; $y/R_a \sim 0.3$, 1.5 and figure 10b), due to the strong interaction of the two jets (i.e. co-annular and swirl jet). Particularly, this phenomenon induces intense oscillations in the outer shear layer (see figure 10b, movie 3). In the far downstream position, after the vortex core centre (VCC), the deficiency in the momentum of two streams leads to a reduction in intensity of these oscillations. Frequency signatures derived from FFT (figure 12a; $y/R_a \sim 3$) are also in line with this argument.

Dynamics of central toroidal recirculation zone (CTRZ)

For the CTRZ case, the dominant mode is identified as centrifugally unstable (see M1 in figure 9b). This is due to the strong influence of the azimuthal shear induced by high swirl ($\rho U_\theta^2 > \rho U_y^2$). Rayleigh's inviscid criterion and the theoretical work done by Coles (1965) state that the shear layer becomes unstable either due to a circulation intensity decrease in the radial direction or due to a stratification in angular momentum.

$$\frac{\mathrm{d}\Gamma}{\mathrm{d}r} < 0; \quad \omega_z \Omega < 0. \qquad (4.1a,b)$$

Hence, the dominance of centrifugal effects in the CTRZ mode is evident from the negative vorticity zone in the central region (figure 9b, M1). The second mode is anticipated as the axial shear mode, which may arise due to the interaction between the inner and outer shear layers (OSL, ISL) induced by vortex bubble breakdown (VBB). Unlike the PVB case, the shedding mode in CTRZ carries a much lower energy (figure 9b, M4). As a result, harmonics are not observed with the shedding mode. All the modes exhibit frequency peaks concentrated around a very narrow band
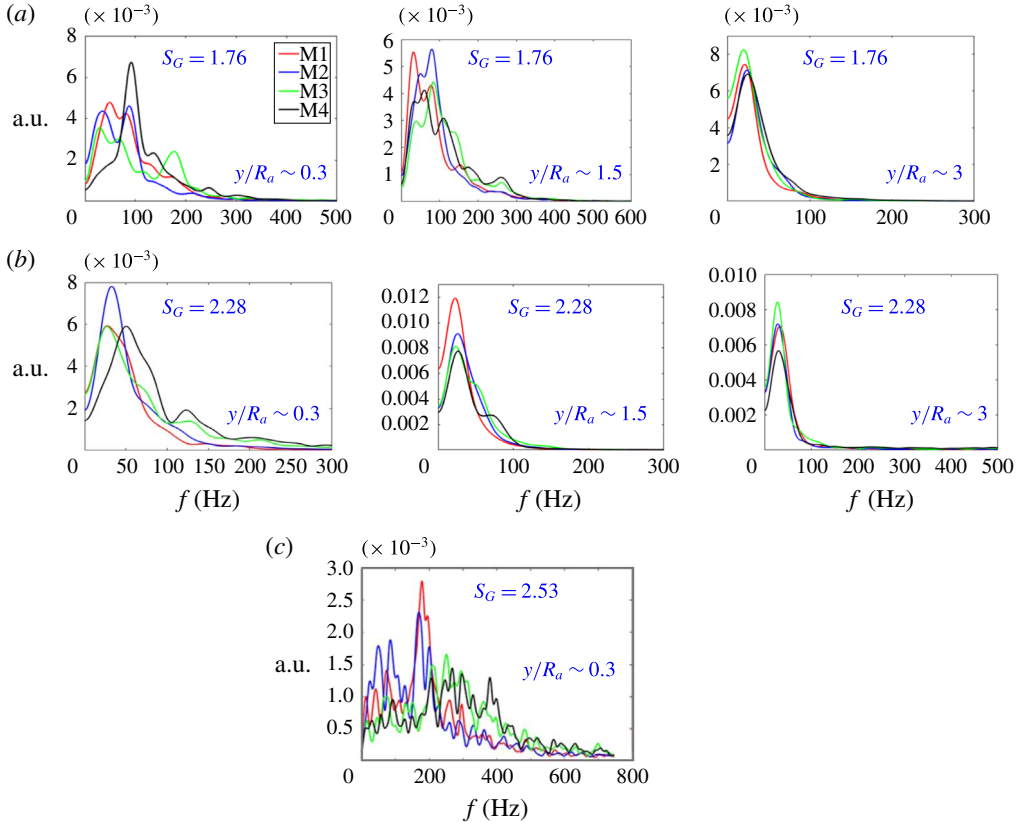
FIGURE 12. (Colour online) Illustration of frequency signatures observed across various axial locations in the r–θ plane ($Re_a \sim 4896$).

of $\sim$10–20 Hz (figure 11b). In general, the helical shear mode exhibits higher energy content for flows with weak swirl (i.e. prior to VBB). However, CTRZ exhibits strong vortex breakdown; hence the helical mode appears as the third mode (figure 9b, M3).

Contrary to observations made for PVB in the r–θ plane, with the CTRZ flow mode, for all y–R_a planes, activation of the shedding mode is not perceived. The frequency signatures of CTRZ pertaining to the VCC plane show dual peaks in mode 1 (figure 12b, $y/R_a \sim 1.5$). This may due to mild oscillations induced by the precessing vortex core (PVC). It is well known that PVC in strong swirling jets (the ones which exhibit VBB) induces oscillations in the flow (Syred 2006; Oberleithner *et al.* 2015). However, in a global sense, azimuthal and axial shear modes appeared to be the most energetic flow modes in the CTRZ conditions (see figures 9b and 10c).

Dynamics of conical breakdown (CB)

The spatial eigenmodes pertaining to the conical breakdown case is shown in figure 9(c). Contrary to the PVB and CTRZ conditions, the CB case shows highly energetic shedding structures (see figure 9c, M1). Here, almost all of the four modes show the dominance of shedding vortices. The dominance of shedding structures in CB results in the appearance of frequency harmonics across all of the modes (figure 11c,d). In order to understand the underlying dynamics of CB, POD is implemented over two small intervals of ΔS_G ($\sim$0.05). To achieve this, flow rates across the tangential ports are varied in small steps of $\sim$4 1 min^{-1}. The corresponding

frequency signature is shown in figure 11(c,d) (for eigenmodes figure 11d shows a similar pattern and hence is not shown here). It is seen that in both cases, frequency peaks shifted towards the higher side ~50–100 Hz and exhibit harmonics. Further, it is very interesting to note that for the flow conditions which recover back to CTRZ from CB, the frequency values also shifted to the lower side and harmonics are not evident (figure 11e).

For the CB case, since the breakdown occurs very close to the burner exit with rapid radially outward flow expansion (not in the axial direction), POD in the r–θ plane is computed only in the near-field plane close to $y/R_a \sim 0.3$. The frequency signature at this location delineates the strong dominance of shedding across all modes. In the y–r plane POD, it is mentioned that the sudden shift in frequencies towards the higher side may be the reason why the flow undergoes conical breakdown. The POD analysis carried out in an r–θ plane also shows similar behaviour.

The higher-order frequencies exhibited by the shedding vortices may be the energy source responsible for the conical breakdown. This argument will be further proved by DMD analysis in subsequent sections.

Furthermore, the Mie scattered raw images acquired during time-resolved measurements suggest intense bubble bursting in the central core region (figure 13a–c). The bursting intensifies with an increase in swirl number, until the flow undergoes conical breakdown. At the transition state $(S_G)_{c1}$, although the bubble starts to burst, the flow is still attached to the rotating core (figure 13a,b; see movie 4). However, at the conical breakdown state, the increased centrifugal momentum causes the flow to stay predominantly at the periphery (figure 13c,f). The flow conditions prior/closer to CB are identified as precursor events. We can see severe intermittency in bubble bursts across the temporal space (figure 13g). On account of the intermittency associated with bubble burst, these precursor events exhibit highly unstable behaviour with shear layer oscillations observed across longitudinal (y–r) and azimuthal (r–θ) planes.

The above-mentioned observations are clearly delineated in movie 4 (r–θ plane) and movie 5 (y–r plane).

4.1.2. *Influence of sampling frequency*

The frequency signatures perceived from the POD temporal modes corresponding to CB (figures 11d; 12) exhibit a wide band of frequency oscillations in the range of ~100–600 Hz. To precisely probe the existence of any further frequencies beyond this range, experiments have been conducted at higher sampling rates (i.e. ~3.5 kHz; 5 kHz). For instance, the comparison made between the frequency signatures observed across three sampling rates (1.5 kHz, 3.5 kHz and 5 kHz) for $Re_a \sim 17\,456$ is graphically depicted in figure 14.

It is clear that in all the cases, the frequency signatures follow a similar trend. Interestingly, as seen from figure 14(c), even at higher sampling rates (i.e. 5 kHz), there are no significant higher-order frequencies. It should be noted that 5 kHz is the maximum attainable sampling frequency used in this study (equipment limitations). Since, the observed maximum frequencies are in the range of $\leqslant$550 Hz, the dynamics extracted from the flow field using a sampling rate of 1.5–5 kHz is reasonable. However, minor shifts in peak frequencies (figure 14 without any loss of major physical insight) can also be partially attributed to the limitation in sampling rate. In addition, a lower sampling rate may cause undetected high frequency signatures (although this is unlikely in the current set of experiments) in swirling flows. Furthermore, it should be noted that we have observed a slight variation (~10–15 Hz)
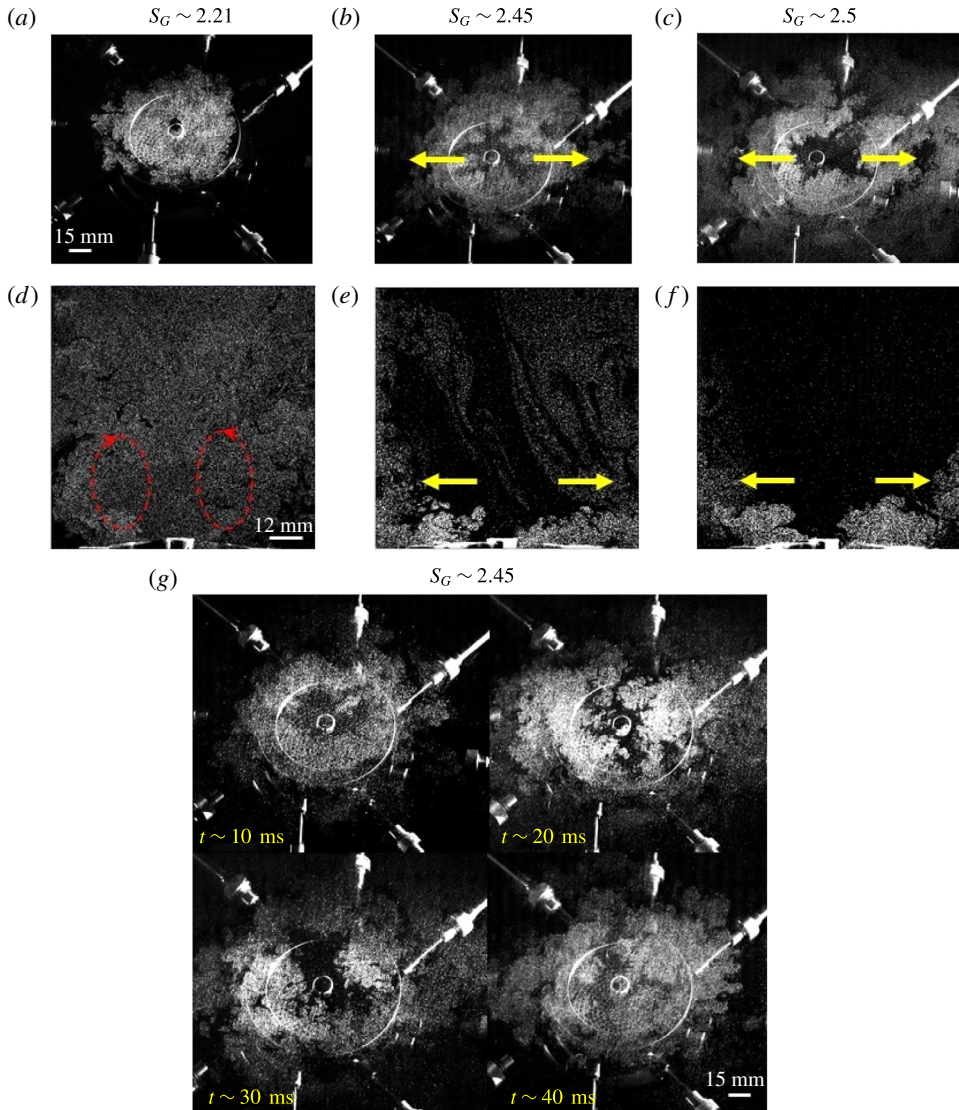
FIGURE 13. (Colour online) Sequence of PIV raw images illustrating the intense bubble bursting phenomenon in the conditions close to CB.

in the dominant frequency even when the experiments are repeated for the CB case at the same sampling rate. However, these variations are very minimal/negligible for the CTRZ and PVB cases. Hence, the slight difference in frequency (noticed in figure 14*a–c*) is attributed as an effect of unsteadiness associated with the CB mode itself. However this slight difference could also be partially due to the limited sampling rate. In particular, CB is always known to induce severe oscillations in the outer shear layer, which further induce multiple shedding vortices in the shear layer. This has been reported by Billant *et al.* (1998) through smoke flow visualization experiments. Billant *et al.* (1998) also showed the intermittency in the emptying and filling process of fluid inside the recirculation zone. In addition, their hysteresis analysis delineated the evolution to variations in the temporal dynamics of conical breakdown.
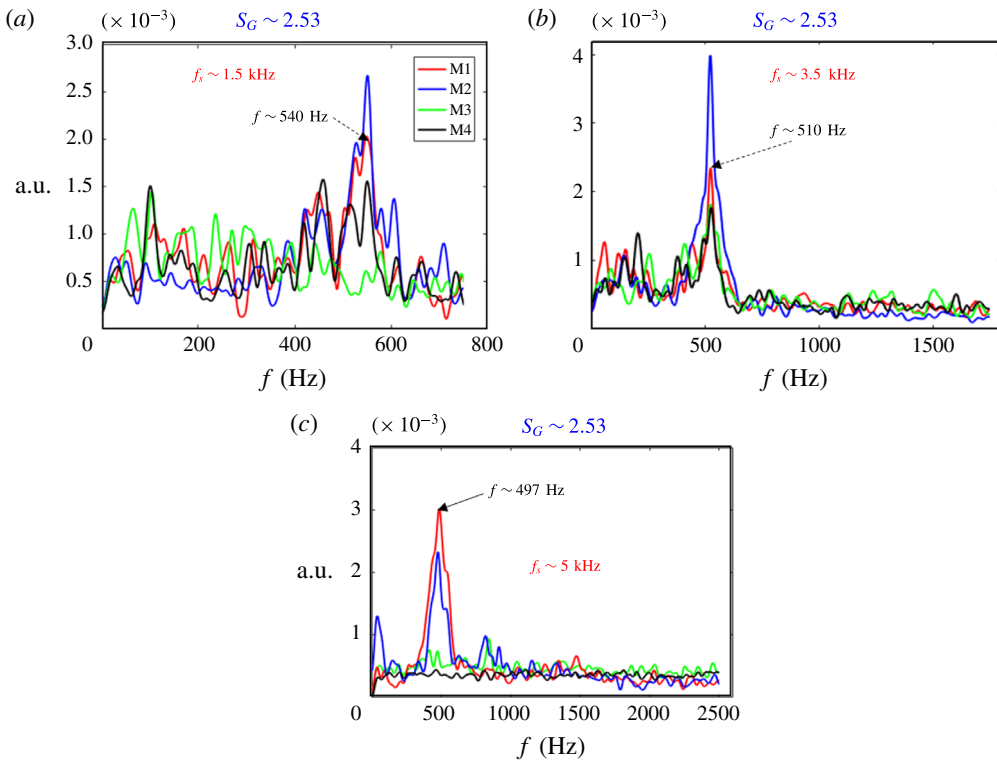
FIGURE 14. For caption see next page.

Owing to the low bulk velocity of the flow ($U_o \sim 1.23$ m s^{-1}, 2.497 m s^{-1}, 4.01 m s^{-1} respectively at $Re_a \sim 4896$, 10 545, 17 546), we have found that temporally ~ 2 s of data are needed to achieve a proper temporal average of the flow field. This is particularity significant with the low Re_a case. For instance, the time-averaged streamline plot of $Re_a \sim 4896$ sampled at 3.5 kHz (see figure 14c) shows an erroneous temporal average mainly due to the reduction in the sampling time. The lowering of the sampling time occurs due to the limitation of the on board storage of the camera at 3.5 kHz sampling. Therefore, acquisition of images at 1.5 kHz becomes more of an optimum choice for the present study.

4.2. *Identification of robust modes using dynamic mode decomposition*

In the previous section, POD has been employed to elucidate the energetic structures present in each vortex breakdown mode. In general, POD is viewed as a modal reduction technique which quantifies the dominant structures that govern the flow field (Taira *et al.* 2017), or in simple terms, it is basically an 'energy ranking method'. Several researchers have quoted that although POD precisely resolves the dominant spatial structures, it may be difficult to predict the contribution of each frequency in the flow field. For instance, M2 in figure 12(c), shows multiple frequency values. Likewise, other modes also show several frequency values. Hence, from POD analysis, it is too cumbersome to predict the contribution of a particular frequency value towards the dynamics/stability of the flow. Recently however, another modal analysis technique named dynamic mode decomposition (DMD) has received
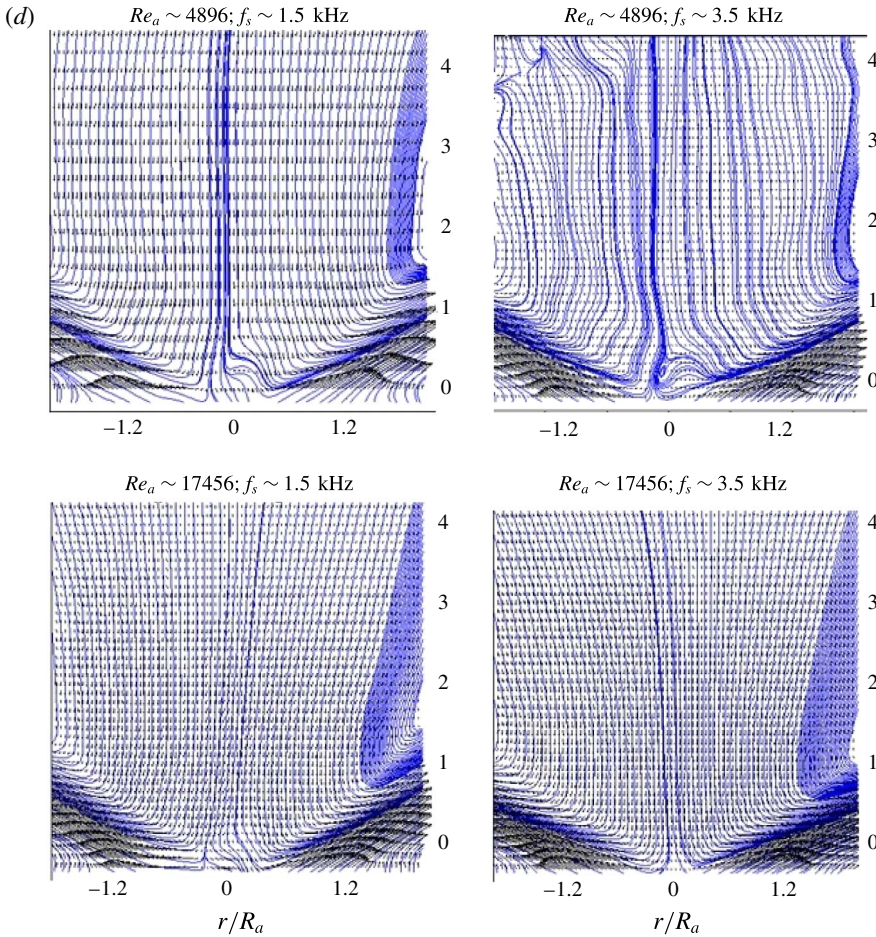
FIGURE 14. (cntd). (Colour online) Comparison between frequency signatures observed at CB case for $Re_a \sim 17\,456$. (*a*) 1.5 kHz; (*b*) 3.5 kHz; (*c*) 5 kHz. (*d*) Time-averaged flow field acquired as various sampling rates.

greater attention in the understanding of the dynamics of a given flow field. This technique was originally developed by Schmid (2010) and later improved in several ways by many researchers (Williams, Kevrekidis & Rowley 2015; Proctor, Brunton & Kutz 2016). The essential role of DMD is to evaluate the contribution of each frequency found in the flow field. In essence, it attempts to predict whether a particular frequency forces the flow to become stable or unstable. More details on the strengths and weaknesses of modal analysis tools like POD, DMD, single value decomposition (SVD) etc. in interpreting fluid flows are elaborated with illustrative examples in Taira *et al.* (2017).

4.2.1. *Implementation of DMD*

In the first step, the acquired set of instantaneous snapshots (i.e. velocity fields) needs to be converted into a matrix form. In particular, the velocity data set pertaining to each instant of time should be represented in a sequential way (i.e. over '*n*' time instants) in the form of a column matrix:

$$\boldsymbol{X}_1^N = \{v_1, v_2, v_3, \ldots\ldots, v_N\}. \tag{4.2}$$

The matrix obtained using (4.2) from instantaneous data sets can be further treated as follows

$$\boldsymbol{X}_1^{N-1} = \{v_1, v_2, v_3, \ldots\ldots, v_{N-1}\}, \tag{4.3}$$

$$\boldsymbol{X}_2^{N} = \{v_2, v_3, v_4, \ldots\ldots, v_N\}. \tag{4.4}$$

Now, the constant linear mapping or dynamical propagator Y needs to be defined to represent the velocity fields at each time instant

$$v_{k+1} = Yv_k, \tag{4.5}$$

$$\boldsymbol{X}_2^{N} = Y\boldsymbol{X}_1^{N-1}. \tag{4.6}$$

The single value decomposition of (4.2) yields,

$$\boldsymbol{X}_1^{N-1} = \boldsymbol{U}\boldsymbol{S}\boldsymbol{V}^J, \tag{4.7}$$

$$\boldsymbol{X}_2^{N} = \boldsymbol{U}\boldsymbol{S}\boldsymbol{V}^J\boldsymbol{X}_1^{N-1}, \tag{4.8}$$

$$Y = \boldsymbol{U}^J\boldsymbol{X}_2^{N}\boldsymbol{V}\bar{\boldsymbol{S}}. \tag{4.9}$$

Here, $\boldsymbol{U}$, $\boldsymbol{V}$ are orthonormal matrices and $\boldsymbol{S}$, $\bar{\boldsymbol{S}}$ represent the diagonal and pseudo-inverse of the diagonal matrix respectively.

Finally, the diagonal matrix with eigen values (μ) is obtained. Further, these values are converted to Floquet values as follows

$$\omega = \frac{\ln(\mu)}{\Delta t}, \tag{4.10}$$

where, Δt is the time separation between successive frames/snapshots.

The parameter ω is represented as a combination of real and imaginary parts ($\omega = \omega_r + \omega_i$), from which frequency can be extracted as follows

$$f = \frac{\omega_i}{2\pi}. \tag{4.11}$$

The value and sign of ω is used as a criterion to analyse the dynamics of the flow. For instance, positive and negative values of ω denote unstable and stable modes respectively. In general practice, modes (modes 1, 2, 3, $\ldots$, n) in the DMD are interpreted based on the magnitude of ω in descending order. Recently, ranking the DMD modes based on their amplitude coefficients (derived using the least squares method) has become popular. The mathematical procedure involved with sorting the DMD modes based on modal amplitude is illustrated with details in Rowley *et al.* (2009) and Mohan, Gaitonde & Visbal (2015). DMD usually assigns the highest growth rates to the flow with small-scale eddies originating from wakes, even though these eddies possess less energy. In applications where the objective is to find the dynamic nature of the frequency associated with energetic coherent structures, DMD modes ranked based on amplitude are highly preferred. To illustrate this phenomenon, comparison is made between the growth rate (ω_r) and amplitude (ξ) based DMD modes (figure 15) for the CTRZ case at $Re_a = 4896$.

The DMD computed based on the growth rate algorithm shows a dominant value around ~ 400 Hz (marked as 'j' in figure 15a (ii)), whereas the amplitude versus frequency plot shows dominance around ~ 30 Hz. The spatial modes corresponding to the frequencies marked with i, j, k in figure 15(a) (ii), (iii) respectively are shown
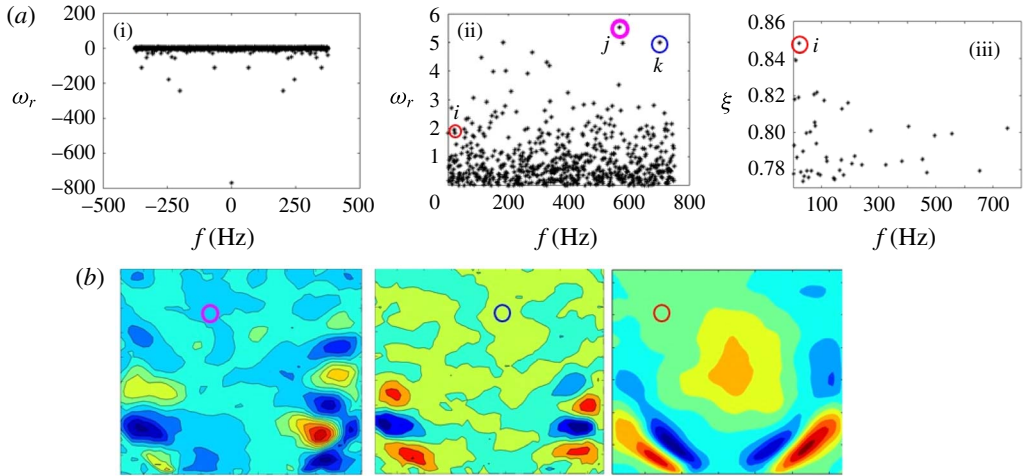
FIGURE 15. (Colour online) (*a*) Illustration of comparison between dynamic modes
extracted using growth rate versus amplitude based algorithms: (i) DMD growth rate
versus frequency; (ii) DMD growth rate (only unstable) versus frequency; (iii) DMD
amplitude versus frequency. (*b*) Spatial modes corresponding to the frequencies marked
with *i, j, k* in (*a*).

in figure 15(*b*). The spatial modes clearly delineate that the higher-order frequencies
shown by the growth rate algorithm are contributed by the outer shear layer shedding
in the flow. On the contrary, the frequency values ranked based on the amplitude (ξ)
show that the shear mode is dominant which is identified as a most energetic mode
in the POD analysis. This clearly delineates the disclaimer associated with (ω_r) and
(ξ) in identifying the dominant modes in the given flow field.

Since, in this study, the main objective is to identify the fluid dynamic cause
behind various transition and flow modes (which are believed to be mostly governed
by dominant coherent structures in the flow field), we have computed DMD modes
based on modal amplitudes ξ.

The obtained DMD modes across various swirl numbers for $Re_a = 4896$ are
graphically illustrated in figure 16. It should be noted that the only first fifty modes
(frequency) sorted based on amplitude (ξ) are shown. For brevity, the frequencies
pertaining to the *y–r* plane are shown in figure 16. However, the comparison
between frequencies corresponding to ξ_{max} observed across the *y–r* and *r–θ* planes is
graphically depicted in figure 18(*a*).

4.2.2. *Insights into the vortex breakdown dynamics using combined POD and DMD
analysis*

In general, DMD modes are compared with POD modes by extracting the spatial
structure pertaining to each frequency obtained in the DMD spectrum. This is to
corroborate whether the energy content of the spatial structure pertaining to the
dominant frequency in the DMD plot is physically relevant or not. For instance, the
spatial structure (shown in figure 17*a*; $S_G \sim 2.28$) corresponding to f_1 of $S_G \sim 2.28$
(figure 16) is similar to M1 in figure 9(*b*), can be interpreted as showing that the
corresponding flow condition is dominated by the KH shear instability.

The frequency signature plotted against amplitude (ξ) delineates the rapid shift of
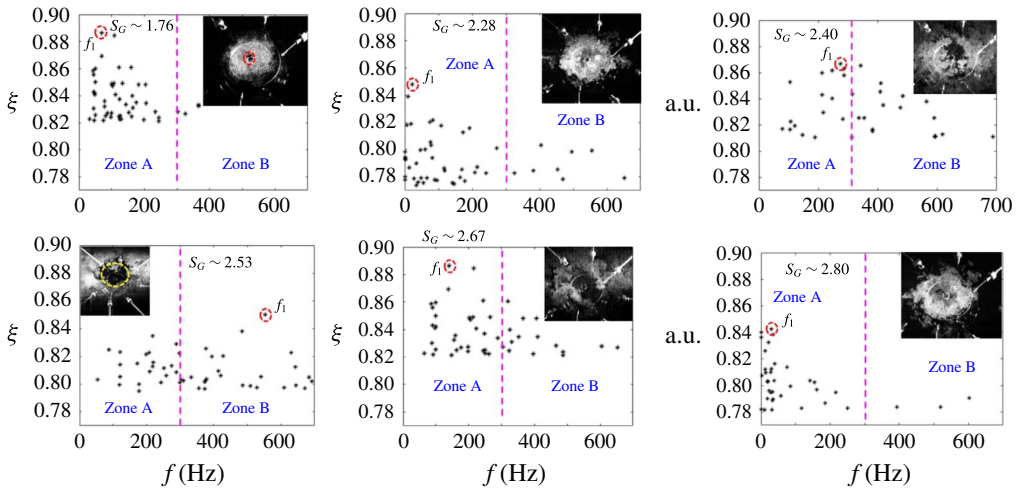f_1 towards higher values (300–50 Hz) when the flow approaches conical breakdown

FIGURE 16. (Colour online) DMD amplitude ranked frequency signatures across various S_G values in the y–r plane ($Re_a \sim 4896$).

(see $S_G \sim 2.40$, 2.53 in figure 16). However, for the other cases, it is clear that the dominant frequency f_1 concentrates around <100 Hz (marked as zone A). Particularly for pre- and post-CTRZ cases, f_1 is observed around ~ 30 Hz. Though, all the cases show some frequencies in the range of 300–500 Hz, excepting the CB case, the same is not observed within the first 20 DMD modes.

As mentioned earlier, it is necessary to evaluate the spatial structure pertaining to f_1 to yield quantitative information on the dynamics governing each flow state (i.e. PVB, CTRZ, CB). The reconstructed spatial structures of f_1 resemble the most dominant (M1) spatial eigenmodes perceived from POD analysis (see M1 in figures 9a–c and 10a,b). The spatial structures of the higher-order frequencies observed with CTRZ, PVB predominantly show shedding which is identified as low energetic structures (% TKE $\sim 15\%$) in POD reconstruction. Hence, the contribution of higher-order frequencies with these flow conditions (i.e. CTRZ, PVB) is insignificant.

Furthermore, the energy ratio (ψ) between the shedding and shear modes is computed to quantitatively represent the contribution of spatial structures in the given flow conditions. The parameter ψ can be defined as follows,

$$\psi = \frac{(\% \ \text{TKE})_{shedding}}{(\% \ \text{TKE})_{shear}}. \tag{4.12}$$

The energy ratio (ψ) calculated across various S_G values are graphically illustrated in figure 18(b). Additionally, only peak frequencies (i.e. f_1) obtained from the DMD plot are also shown in tandem (figure 18a). The values clearly demarcate, that with the swirl number increasing from 1.5 to 3, the frequencies show a sudden rise in a very narrow band ($S_G \sim 2.45$–2.55). Correspondingly, the energy contribution of the shedding modes also shows a sharp peak in this zone. Hence, it is interpreted that the occurrence of the sudden rise in the higher-order frequencies together with the dominant nature of shedding mode causes the flow to undergo conical breakdown. Further, figure 18(a,b) is constructed in the form of a regime map from which states of various flow modes under the influence of S_G can be identified.
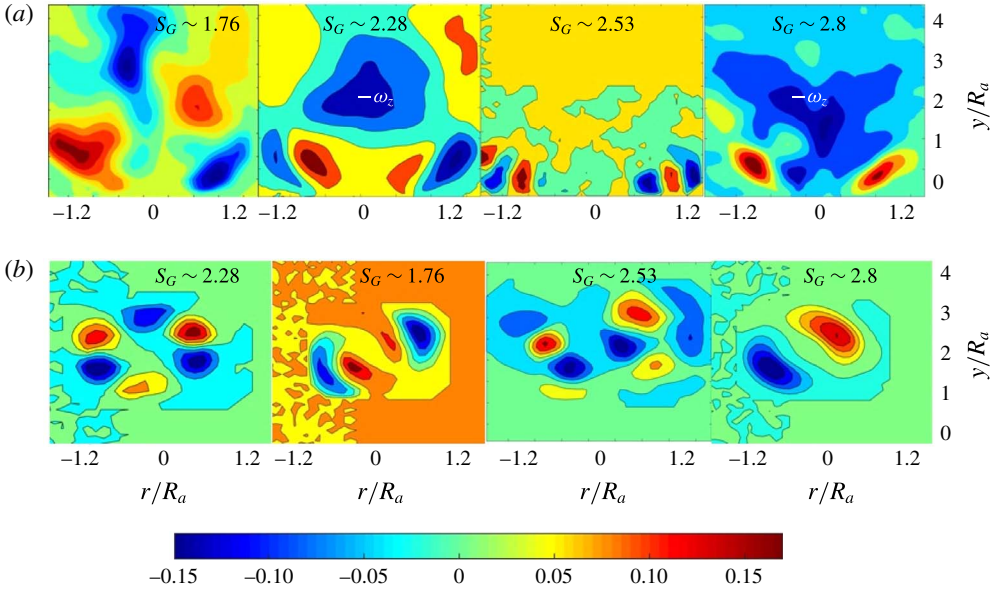
FIGURE 17. (Colour online) Robust dynamic modes observed across various vortex breakdown modes. (*a*) *y–r* plane; (*b*) *r–θ* plane at $y/R_a \sim 0.3$ ($Re_a \sim 4896$).
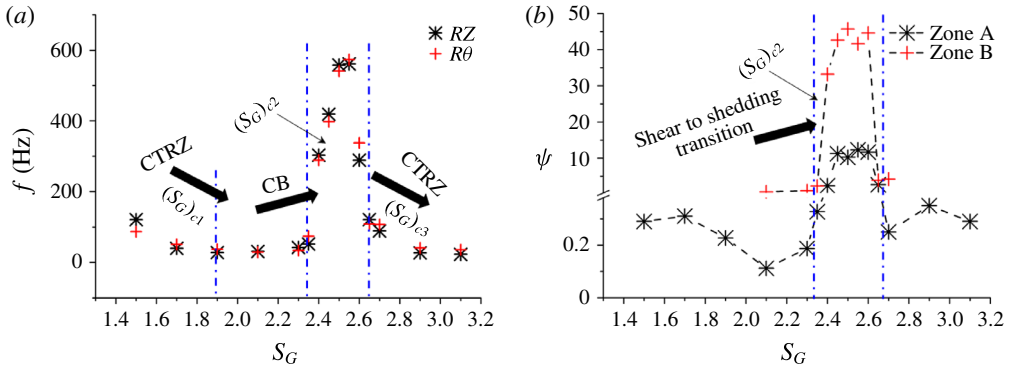

FIGURE 18. (Colour online) (*a*) DMD-based amplitude ranked frequencies across various S_G values; (*b*) energy-ranked VB modes derived from POD analysis ($Re_a \sim 4896$).

The observations made with POD and DMD analysis can be summarized as follows

$$f_1 \leqslant 100; \; \psi < 1 \rightarrow PVB, CTRZ, \tag{4.13}$$

$$f_1 \geqslant 300; \; \psi \gg 1 \rightarrow CB. \tag{4.14}$$

4.3. *Conical breakdown mechanism*

The understanding related to the occurrence of conical breakdown in swirling flows still remains hypothetical since the first report made by Billant *et al.* (1998) and later by Santhosh *et al.* (2013) although extensive works (Benjamin 1962; Sarpkaya 1971*b*; Hall 1972; Leibovich 1978) have been reported on the vortex breakdown phenomenon

in swirling flows, occurrence of CB is not understood clearly. Billant *et al.* (1998) showed that flow undergoes CB if the pressure at the stagnation point and the ambient are identical. This essentially shows the absence of steady motion between the fluid in the stagnation zone and the ambient fluid. In general, when the flow is moving towards a higher swirl number, first helical vortices appear in the flow at moderate S_G followed by bubble breakdown at higher S_G. The transfer of energy from the azimuthal waves to the helical waves is viewed as a source for vortex bubble breakdown at higher S_G values.

In the present study, the combined DMD and POD analyses carried out over the time-resolved PIV data acquired at various y–r and r–θ planes reveal the dominance of shedding modes at the onset of conical breakdown. In general, although shedding is observed at the outer shear layer (OSL) across all flow conditions, its intensity may be reduced due to the presence of strong shear induced by two counter-rotating eddies in the near field (see figure 3). This can be viewed as a holder for OSL shedding, whereas in the CB case, the flow is not constrained by these two counter-rotating eddies (figure 3; $S_G \sim 2.53$). The flow starts to shed from the burner exit itself. The vanishing nature of the counter-rotating eddies are clearly visible in the flow case close to CB (figure 3; $S_G \sim 2.4, 2.67$). Furthermore, this can also be interpreted from the DMD spectrum shown in figure 16, for instance, higher-order frequencies (say >300 Hz) do appear for PVB, CTRZ but the strong shear (axial + azimuthal) induced by counter-rotating vortices prevents the flow from undergoing conical breakdown.

The present and previous investigations clearly delineate that temporally, the CB state undergoes oscillations attributed to strong shear layer shedding. Previous studies (Chanaud 1965; Spall *et al.* 1987) have proved that swirl flow undergoes vortex breakdown if and only if the magnitude of R_O is less than 1. Although CB always appears in the azimuthal momentum dominant condition (i.e. $R_O < 1$), it happens over a very narrow band and quickly recovers back to CTRZ even when the flow rate is continuously increased, favouring azimuthal momentum. However, the issues which remain as hypotheses relate to why conical breakdown happens in the very narrow band and why it recovers back to the classical CTRZ mode.

The occurrence of conical breakdown in a narrow band can be hypothesized as follows.

In general, swirl flows exhibit instability waves in the azimuthal as well as axial direction. The classical CTRZ structure in swirl flow is an evolution resulting from helical waves occurring at low swirl number. Stability analysis performed with swirling jets clearly delineates the evolution of various forms of shear layer instability mechanisms as a function of S_G (Afanasyev & Peltier 1998; Gallaire & Chomaz 2003a). The results presented by Gallaire & Chomaz (2003a) reveal the activation of centrifugal instabilities in addition to KH (axial + azimuthal) instabilities even with the presence of axial plug flow.

Likewise, in the present study, an increase in S_G from the CTRZ mode may predominantly pump energy into azimuthal waves rather than into axial KH waves ($\lambda_\theta > \lambda_{axial}$). The highly energetic unstable waves induced in the azimuthal plane may cause the flow to fan out completely (see figure 20a). At the instant of CB, the raw images clearly suggest that the axial jets are completely engulfed by the coaxial swirling jet. Moreover, the raw images pertaining to pre- and post-CB also suggests that the instability waves induced due to shear inside the jet (position where the swirl jet interacts with the axial jets) are not intensified (see figure 19b). However, during CB, the waves are clearly visible at the inner and outer surface of the jet (figure 19a). This may be due to the dominance of centrifugal instabilities as pointed
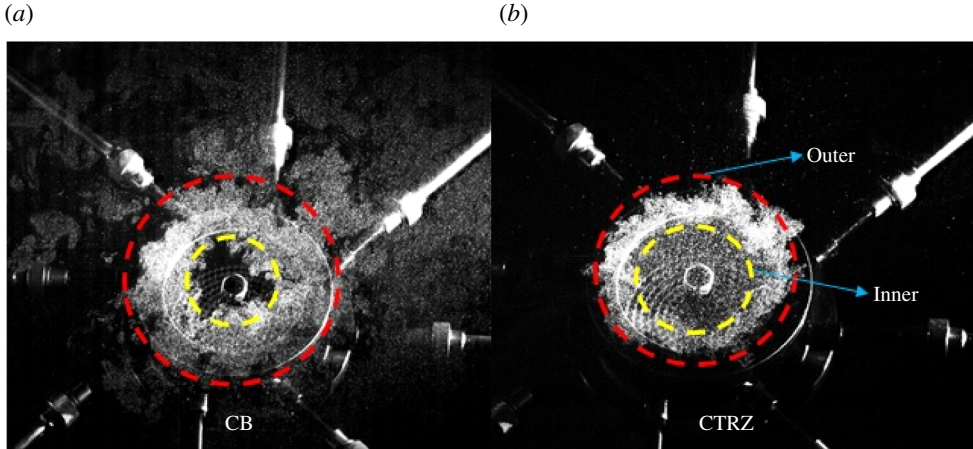
(*a*)   (*b*)

FIGURE 19. (Colour online) Schematic illustration of shear waves formed at inner and outer surfaces of the jets.

out by Gallaire & Chomaz (2003*a*) in their stability analysis. However, the resultant flow structure during the dominance of centrifugal instabilities is not shown in Billant *et al.* (1998).

The force induced by axial and azimuthal waves can be written as follows

$$F_{KH_{axial}} \sim \rho U_o^2 / \lambda_{axial}, \qquad (4.15)$$

$$F_{KH_\theta} \sim \rho U_o^2 / \lambda_\theta. \qquad (4.16)$$

Beyond CB, a perturbation caused to the flow in terms of increased S_G might result in the damping of azimuthal waves (λ_θ; $F_{KH_{axial}} > F_{KH_\theta}$). The occurrence of this event in the small S_G space clearly delineates CB as a highly unstable phenomenon. It should be noted however that the above discussed argument is purely a hypothesis. To precisely probe the mechanism of conical breakdown (particularly to answer why it occurs in a very narrow band), it is necessary to acquire the three-dimensional flow field data in a simultaneous fashion to check for the evolution of vortices in the spatial domain. In swirling flows, the momentum will be spread in the azimuthal as well as axial direction (figure 20*c*). As a result, azimuthal and axial shear waves will be induced in the flow field. In addition, Garcia-Villalba, Frohlich & Rodi (2005) and Komarek & Polifke (2010) have identified the 'indirect mechanism' by which axial vorticity is excited, which ultimately results in fluctuations in the waves. The influence of these waves as flow transits to CB from the CTRZ state can be identified only if these wavenumbers are identified in a quantitative fashion. However, these demand either three-dimensional flow field data or a rigorous three-dimensional stability analysis (Oberleithner *et al.* 2011), which are not within the scope of this manuscript.

It should be noted that the present study is not aimed at a quantitative understanding of why conical breakdown occurs in a narrow band. Rather, we are more focused on how the flow dynamics evolves as the flow approaches and passes the conical breakdown states. Even with the limitations of time-resolved two-dimensional PIV measurements, we have precisely delineated the precursor events such as the activation of multiband oscillations when the flow approaches the CB state. This information provides more insights into dynamical features of CB rather than the mechanism
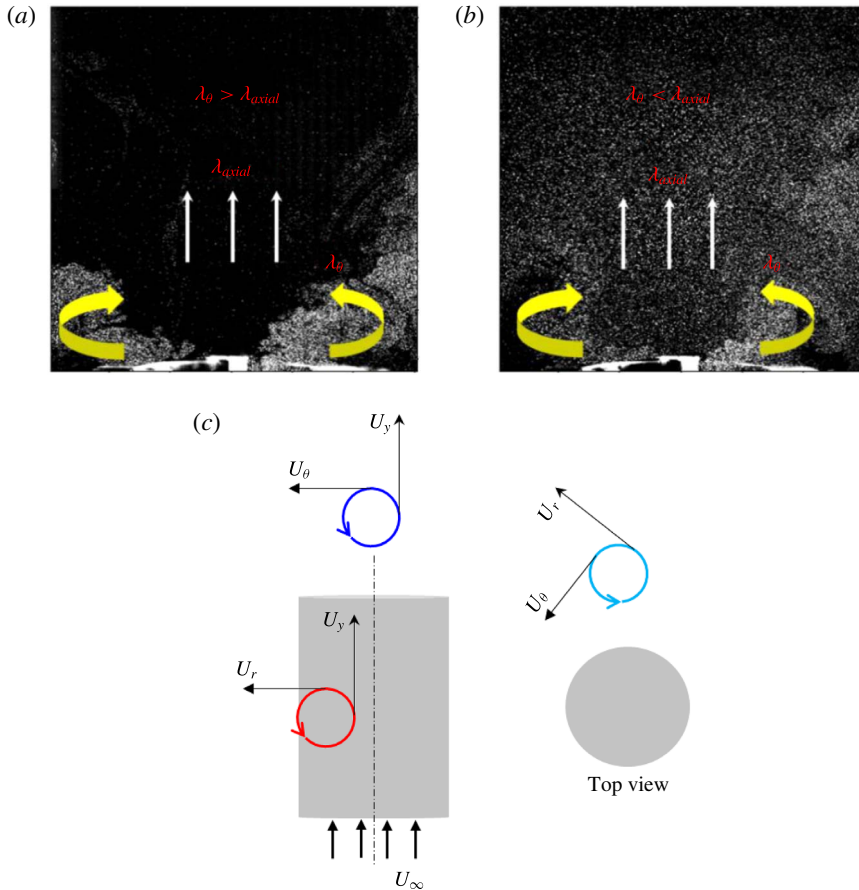
FIGURE 20. (Colour online) Hypothetical illustration of azimuthal and axial instability waves. (*a*) Conical breakdown; (*b*) CTRZ; (*c*) spatial evolution of vortices in swirling flow field.

which governs its formation. This feature has not documented in the literature to date.

Furthermore, while progressively inducing swirl in the axial jets, the flow exhibits strong helical waves followed by vortex breakdown at high swirl number. At the instant of CB, helical waves might vanish completely due to centrifugal effects and may result in the flow detaching from the vortex core. However, to validate this point, three-dimensional flow field data are required to visualize the evolution of helical waves while S_G is progressively varied.

Moreover, CB is also observed with a similar type of test rig which discharges swirl flow through a vane swirler. Here also CB appears within a very narrow band when the flow across the swirler is progressively varied (see movie 6). This observation indicates that the occurrence of CB in coaxial swirling flow may be a universal phenomenon. Furthermore, it should be very interesting to note that in both the experiments, CB is witnessed only with the presence of co-annular axial jets. We have not observed any CB in the absence of axial jets, even when the swirl number is progressively varied in very small steps. This clearly indicates that the switching between various instability modes across coaxial jets may cause the flow to undergo conical breakdown.
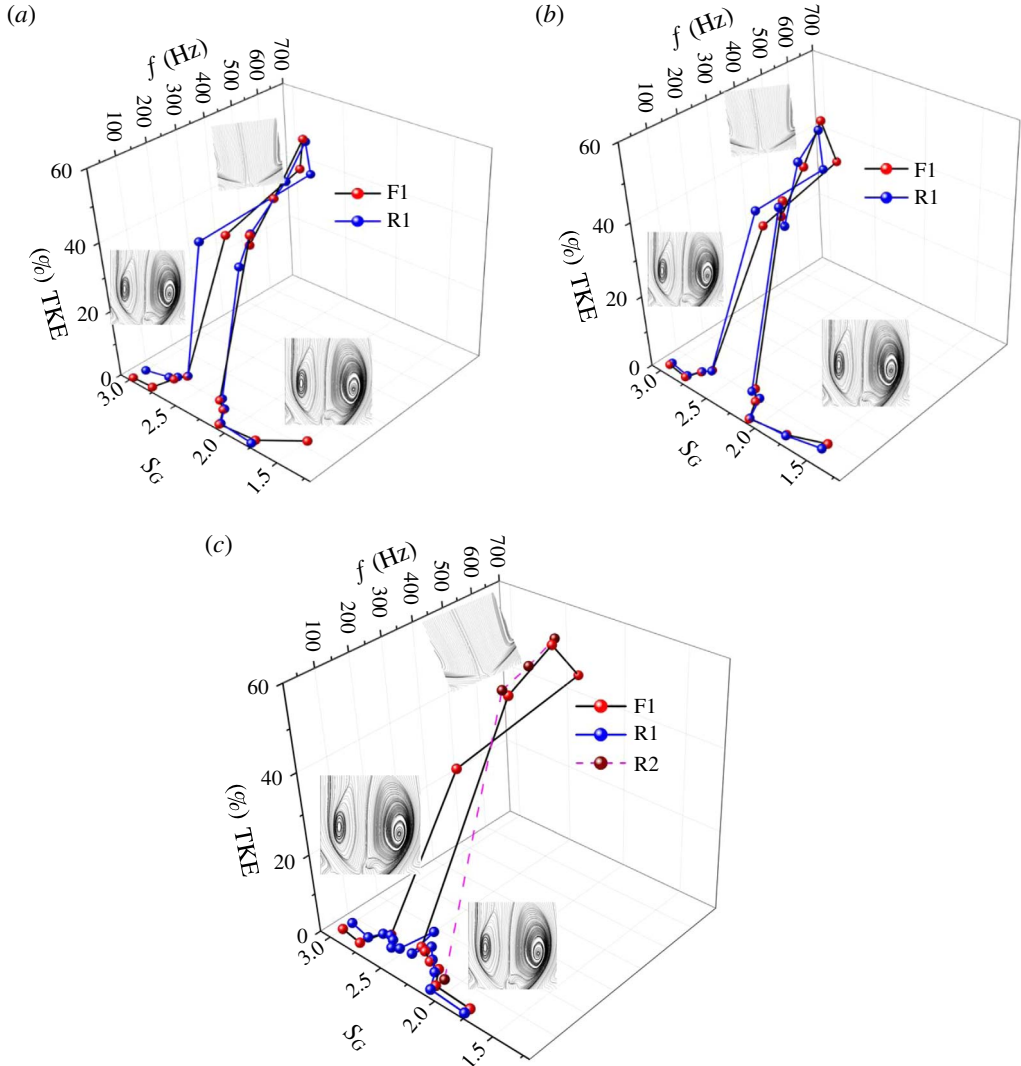
FIGURE 21. (Colour online) Hysteresis phenomenon associated with conical breakdown pathways. (*a*) $Re_a \sim 4896$; (*b*) $Re_a \sim 10\,545$; (*c*) $Re_a \sim 17\,456$.

In both cases, the cone undergoes a series of temporal oscillations in the azimuthal as well as axial direction, which ultimately leads to the dominance of the shedding mode. Previous studies attempted to distinguish CB from other forms of vortex breakdown based on the theoretical arguments deduced from pressure gradients in the flow (Billant *et al.* 1998; Santhosh *et al.* 2014). However, the time-resolved PIV measurements carried out in this study yield new insights into the dynamics of conical breakdown.

4.4. *Hysteresis phenomenon in conical breakdown pathways*

In the global observation section, it was stated that though the time-averaged flow field is similar across all Re_a, the vortex breakdown pathways exhibit contradictory
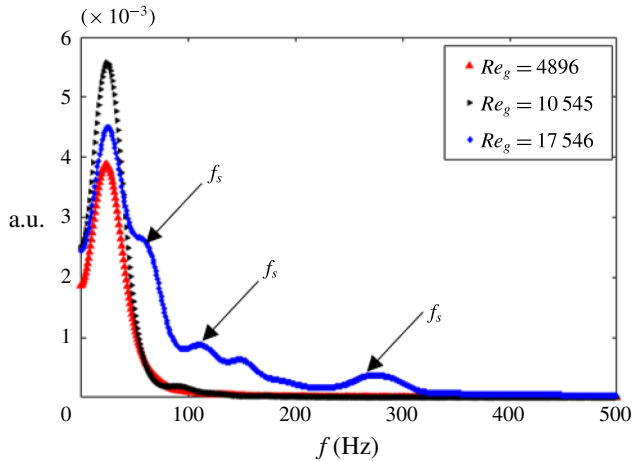
FIGURE 22. (Colour online) Frequency spectrum observed for CTRZ case across various Re_a values.

behaviour. Particular emphasis is placed on the repeatability associated with the conical breakdown state from CTRZ. To illustrate this phenomenon, experiments have been meticulously carried out in a forward (F) and backward (R) manner, i.e. S_G values increased from 1.5 to 3 or decreased from 3 to 1.5 (this can also be interpreted as pre- and post-CTRZ).

The observations are transformed into a three-dimensional map as illustrated in figure 21. Two parameters namely % TKE (from POD) and frequency pertaining to ξ_{max} of DMD are considered across various S_G. These experiments are carried out with very close variation in ΔS_G values ($\sim \pm 0.05$).

From POD and DMD analyses, it is clear that the activation of the higher-order frequencies contributed by shedding eddies in the flow leads to the CB state. Hence, in figure 21, % TKE is considered for the shedding mode. The values of other modes are assigned as zero. For the $Re_a \sim 4896$ case, during the forward set of experiments, conical breakdown starts to appear at $S_G \sim 2.4$ and is observed until $S_G \sim 2.6$ (figure 21a F1). Progressive decrease in S_G from 3 to 1.5 follows the same path (figure 21b R1) in terms of flow topology. Whereas, for $Re_a \sim 17\,456$, the flow path to the CB state during the forward direction is completely different from the backward direction. In the forward condition, the flow undergoes CB around $S_G \sim 2.4$–2.6 and transits back to the CTRZ state, whereas during the backward case, there is no evidence of conical breakdown (figure 21b R1, see blue circles). It should be noted that the activation of higher-order frequencies, which is believed to be a cause for CB, also does not appear with a decreasing value of S_G. However, CB is observed (shown as pink dashed lines in figure 21b) only for a sudden and large decrease in S_G (i.e. $\Delta S_G \sim -0.5$) for $Re_a \sim 10\,545$. The hysteresis analysis performed by Billant *et al.* (1998) reports that CB appears in forward as well as backward cases. This may be due to the low Reynolds number, as is the case for $Re_a \sim 4896$. Their analysis also pointed out the upward and downward shift of stagnation points during forward and backward conditions respectively. It should be noted that upshift of the stagnation point during flow conditions near to CB was already elucidated in the global observation section (see figure 3).

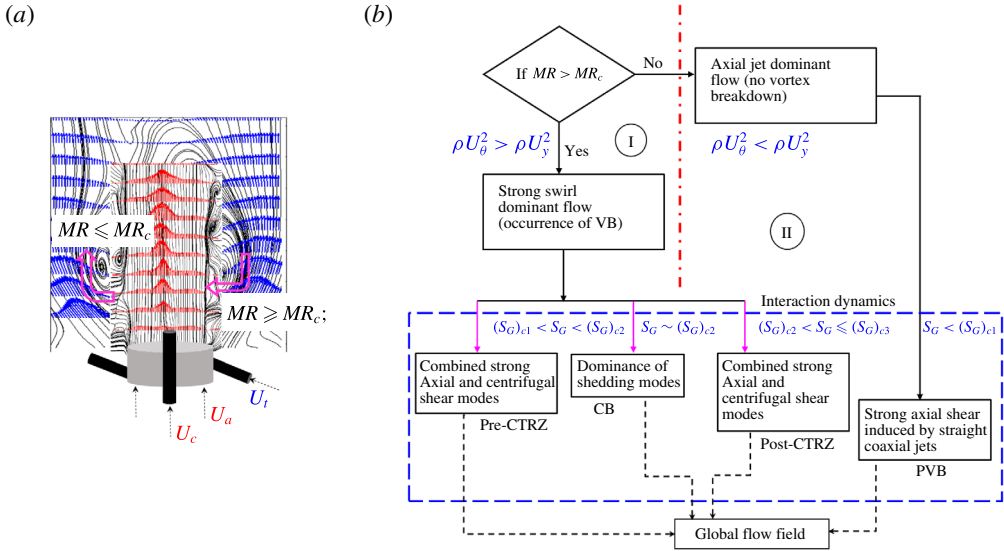(*a*)   (*b*)

FIGURE 23. (Colour online) Illustration of key governing mechanisms observed across various vortex breakdown (VB) modes.

The hysteresis observed at high Re_a may be due to the insufficient residence time (τ_r) associated with the flow.

For instance, if the flow is provided with a higher residence time at $Re_a \sim 17\,456$ as compared to $Re_a \sim 4896$, then CB is also possible in the backward path. Furthermore, it should be noted that, although the CTRZ mode exhibits a dominant frequency around ~ 24 Hz across all the Re_a values, some secondary frequency peaks are observed at $Re_a \sim 17\,456$ (see figure 22). These may be attributed to the small-scale shedding eddies in the flow field, which are intensified due to the higher Re_a.

5. Summary and conclusions

The new insights into the dynamics of the vortex breakdown mechanisms in coaxial swirling flows have been addressed with the help of high fidelity time-resolved laser diagnostic tools. In particular, for the first time, we have reported the fluid dynamic phenomenon governing the special form of breakdown named 'conical breakdown' in swirling flows. In this study, three co-annular flow Reynolds numbers (Re_a) are chosen, and for each Re_a, the swirl number has been progressively varied independently. The global observation outlined in § 3 delineates the time mean transition of the flow field across various S_G values. In addition, it also yields an understanding of momentum transfer pathways across three coaxial jets (A–C).

The summary of the detailed observations presented across various sections is pictorially depicted in figure 23. In a global sense, the flow field considered in this study can be viewed in two major categories i.e. centrifugal momentum dominant flow (I) and axial momentum dominant flow (II). In addition, the flow under region I can be subdivided into four major paradigms (pre-CTRZ, CB, post-CTRZ; figure 23*b*). In region I, the deficiency of swirl momentum or the dominance of co-annular axial jets ($MR < MR_c$) results in complete engulfment of the swirl jet. On account of the weak swirl strength in this regime, the flow does not undergo vortex breakdown.

On the other hand, strong vortex breakdown is witnessed in regime II. Furthermore, the flow exhibits different forms of VB as a function of swirl number S_G. In particular, a special form of breakdown named conical breakdown is observed while the swirl intensity (S_G) is progressively varied. Interestingly, CB persists only over a very short internal of S_G values. Beyond this point, the flow recovers back to its previous VB mode (shown as post-CTRZ in figure 23). The global observations pertaining to each VB mode in regime I and II are detailed in § 2.

Subsequently, POD analysis is employed over instantaneous flow field data acquired from time-resolved PIV to extract the dominant spatial structures (in terms of % TKE) across each flow mode. In addition, the frequency signature pertaining to each dominant POD mode is also acquired using FFT methods. The analysis carried out over y–r, as well as R–θ plane data,- yields a canonical understanding of the governing fluid dynamics phenomenon. For instance, the axial shear mode is identified as a predominant energetic structure in regime II (i.e. PVB), though the signature of shedding eddies is also seen albeit that its intensity is observed only in the near field (i.e. the position where all three jets interact). In addition to axial shear, strong azimuthal shear is also witnessed with the flows enlisted under regime I. This is due to the dominance of centrifugal momentum ($MR \geqslant MR_c$). Like PVB, shedding modes appeared as low energetic modes (i.e. mode 4) in pre- and post-CTRZ flow conditions. On the contrary, shedding modes contribute towards much of the TKE ($\sim$50–70 %) in the CB condition. As a result, harmonics are observed with frequency signatures derived from the temporal modes. Interestingly, the flow recovers back to the shear (axial + azimuthal) dominant mode in the post-CTRZ case (similar to the pre-CTRZ case; see figure 23b). The sudden transition in % TKE from shear to shedding modes with CB case is interpreted as a cause for the flow to undergo conical breakdown.

Next, the frequency ranked dominant flow structure identification method named DMD is implemented to quantitatively corroborate the frequency relevance of the energetic structures identified from the POD modes. Here, the frequencies pertaining to each flow condition are ranked based on amplitude (ξ) derived using the least squares method. The results revealed that, for pre-and post-CTRZ, PVB, frequencies with the maximum amplitude predominantly fall in the range of 30–100 Hz. Whereas, the flow conditions relevant to CB exhibit maximum amplitude for higher-order frequencies 330–600 Hz. Furthermore, the spatial structures pertaining to ξ_{max} in the frequency spectrum match with the dominant structures obtained from the POD analysis. The interpretations gained from the DMD and POD analyses show that the activation of higher-order frequencies with significant TKE results in conical breakdown.

Finally, hysteresis analysis is performed to elucidate the repeatability of vortex breakdown modes across various S_G values. In particular, these measurements are done to check whether CB persists in both forward and reverse directions. It is seen that except for low flow rate conditions ($Re_a \sim 4896$), the path followed by CB is different during the forward and reverse conditions. For instance, with higher air flow rates ($Re_a \sim 4896$; 17 456) CB is observed when S_G is progressively increased with an ΔS_G of 0.05. On the contrary, CB is not witnessed in the reverse direction with the same level of decrease in ΔS_G. CB appeared only for a larger reduction in S_G values ($\sim$0.5).

Acknowledgements

Supplementary movies

Supplementary movies are available at https://doi.org/10.1017/jfm.2018.549.

REFERENCES

AFANASYEV, Y. D. & PELTIER, W. R. 1998 Three-dimensional instability of anticyclonic swirling flow in rotating fluid: laboratory experiments and related theoretical predictions. *Phys. Fluids* **10**, 3194–3202.

ARROYO, M. P. & GREATED, C. A. 1991 Stereoscopic particle image velocimetry. *Meas. Sci. Technol.* **2**, 1181–1186.

BENJAMIN, T. B. 1962 Theory of the vortex breakdown phenomenon. *J. Fluid Mech.* **14**, 593–629.

BENJAMIN, T. B. 1967 Some developments in the theory of vortex breakdown. *J. Fluid Mech.* **28**, 65–84.

BERKOOZ, G., HOLMES, P. & LUMLEY, J. L. 1993 The proper orthogonal decomposition in the analysis of turbulent flows. *Annu. Rev. Fluid Mech.* **25**, 539–575.

BILLANT, P., CHOMAZ, J.-M. & HUERRE, P. 1998 Experimental study of vortex breakdown in swirling jets. *J. Fluid Mech.* **376**, 183–219.

CALA, C. E., FERNANDES, EC., HEITOR, M. V. & SHTORK, S. I. 2006 Coherent structures in unsteady swirling jet flow. *Exp. Fluids* **40**, 267–276.

CASSIDY, J. J. & FALVEY, H. T. 1970 Observations of unsteady flow arising after vortex breakdown. *J. Fluid Mech.* **41**, 727–736.

CHAKRABORTY, P., BALACHANDAR, S. & ADRIAN, R. J. 2005 On the relationships between local vortex identification schemes. *J. Fluid Mech.* **535**, 189–214.

CHANAUD, R. C. 1965 Observations of oscillatory motion in certain swirling flows. *J. Fluid Mech.* **21**, 111–127.

CHTEREV, I., SUNDARARAJAN, G., EMERSON, B., SEITZMAN, J. & LIEUWEN, T. 2017 Precession effects on the relationship between time-averaged and instantaneous reacting flow characteristics. *Combust. Sci. Technol.* **189**, 248–265.

CLAYPOLE, T. C. & SYRED, N. 1981 The effect of swirl burner aerodynamics on NOx formation. In *Symposium (International) on Combustion*, pp. 81–89. Elsevier.

COLES, D. 1965 Transition in circular Couette flow. *J. Fluid Mech.* **21**, 385–425.

ESCUDIER, M. P. & KELLER, J. J. 1985 Recirculation in swirling flow – a manifestation of vortex breakdown. *AIAA J.* **23**, 111–116.

FALER, J. H. & LEIBOVICH, S. 1977 Disrupted states of vortex flow and vortex breakdown. *Phys. Fluids* **20**, 1385–1400.

FU, Y., CAI, J., JENG, S.-M. & MONGIA, H. 2007 Characteristics of the swirling flow generated by a counter-rotating swirler. In *43rd AIAA/ASME/SAE/ASEE Joint Propulsion Conference and Exhibit*, p. 5690. AIAA.

GALLAIRE, F. & CHOMAZ, J.-M. 2003a Instability mechanisms in swirling flows. *Phys. Fluids* **15**, 2622–2639.

GALLAIRE, F. & CHOMAZ, J.-M. 2003b Mode selection in swirling jet experiments: a linear stability analysis. *J. Fluid Mech.* **494**, 223–253.

GARCIA-VILLALBA, M., FROHLICH, J. & RODI, W. 2005 Large eddy simulation of an annular swirling jet with pulsating inflow. In *TSFP Digital Library Online*. Begel House Inc.

GUPTA, A. K., LILLEY, D. G. & SYRED, N. 1984 *Swirl Flows*, vol. 488, p. 1. Abacus Press.

HALL, M. G. 1972 Vortex breakdown. *Annu. Rev. Fluid Mech.* **4**, 195–218.

HARVEY, J. K. 1962 Some observations of the vortex breakdown phenomenon. *J. Fluid Mech.* **14**, 585–592.

HUANG, Y., WANG, S. & YANG, V. 2005 Flow and flame dynamics of lean premixed swirl injectors. *Prog. Astronaut. Aeronaut.* **210**, 213.

KOMAREK, T. & POLIFKE, W. 2010 Impact of swirl fluctuations on the flame response of a perfectly premixed swirl burner. *Trans. ASME J. Engng Gas Turbines Power* **132**, 061503.

LEFEBVRE, A. H. 1998 *Gas Turbine Combustion*. CRC Press.

LEIBOVICH, S. 1978 The structure of vortex breakdown. *Annu. Rev. Fluid Mech.* **10**, 221–246.

LIEUWEN, T. C. 2012 *Unsteady Combustor Physics*. Cambridge University Press.

LOISELEUX, T., CHOMAZ, J. M. & HUERRE, P. 1998 The effect of swirl on jets and wakes: linear instability of the Rankine vortex with axial flow. *Phys. Fluids* **10**, 1120–1134.

LOPEZ, J. M. 1990 Axisymmetric vortex breakdown. Part 1. Confined swirling flow. *J. Fluid Mech.* **221**, 533–552.

LUCCA-NEGRO, O. & O'DOHERTY, T. 2001 Vortex breakdown: a review. *Prog. Energy Combust. Sci.* **27**, 431–481.

MARKOVICH, D. M., ABDURAKIPOV, S. S., CHIKISHEV, L. M., DULIN, V. M. & HANJALIĆ, K. 2014 Comparative analysis of low-and high-swirl confined flames and jets by proper orthogonal and dynamic mode decompositions. *Phys. Fluids* **26**, 065109.

MARKOVICH, D. M., DULIN, V. M., ABDURAKIPOV, S. S., KOZINKIN, L. A., TOKAREV, M. P. & HANJALIĆ, K. 2016 Helical modes in low-and high-swirl jets measured by tomographic PIV. *J. Turbul.* **17**, 678–698.

MELIGA, P., GALLAIRE, F. & CHOMAZ, J.-M. 2012 A weakly nonlinear mechanism for mode selection in swirling jets. *J. Fluid Mech.* **699**, 216–262.

MOHAN, A. T., GAITONDE, D. V. & VISBAL, M. R. 2015 Model reduction and analysis of deep dynamic stall on a plunging airfoil using dynamic mode decomposition. In *53rd AIAA Aerospace Sciences Meeting*, p. 1058. AIAA.

OBERLEITHNER, K., SIEBER, M., NAYERI, C. N., PASCHEREIT, C. O., PETZ, C., HEGE, H.-C., NOACK, B. R. & WYGNANSKI, I. 2011 Three-dimensional coherent structures in a swirling jet undergoing vortex breakdown: stability analysis and empirical mode construction. *J. Fluid Mech.* **679**, 383–414.

OBERLEITHNER, K., STÖHR, M., IM, S. H., ARNDT, C. M. & STEINBERG, A. M. 2015 Formation and flame-induced suppression of the precessing vortex core in a swirl combustor: experiments and linear stability analysis. *Combust. Flame* **162**, 3100–3114.

PRASAD, A. K. & ADRIAN, R. J. 1993 Stereoscopic particle image velocimetry applied to liquid flows. *Exp. Fluids* **15**, 49–60.

PROCTOR, J. L., BRUNTON, S. L. & KUTZ, J. N. 2016 Dynamic mode decomposition with control. *SIAM J. Appl. Dyn. Syst.* **15**, 142–161.

RAFFEL, M., WILLERT, C. E., WERELEY, S. & KOMPENHANS, J. 2013 *Particle Image Velocimetry: A Practical Guide*. Springer.

RAJAMANICKAM, K. & BASU, S. 2017a On the dynamics of vortex–droplet interactions, dispersion and breakup in a coaxial swirling flow. *J. Fluid Mech.* **827**, 572–613.

RAJAMANICKAM, K. & BASU, S. 2017b Insights into the dynamics of spray–swirl interactions. *J. Fluid Mech.* **810**, 82–126.

RAJAMANICKAM, K., ROY, S. & BASU, S. 2018 Novel fuel injection systems for high-speed combustors. In *Droplets and Sprays*, pp. 183–216. Springer.

ROWLEY, C. W., MEZIĆ, I., BAGHERI, S., SCHLATTER, P. & HENNINGSON, D. S. 2009 Spectral analysis of nonlinear flows. *J. Fluid Mech.* **641**, 115–127.

ROY, S., YI, T., JIANG, N., GUNARATNE, G. H., CHTEREV, I., EMERSON, B., LIEUWEN, T., CASWELL, A. W. & GORD, J. R. 2017 Dynamics of robust structures in turbulent swirling reacting flows. *J. Fluid Mech.* **816**, 554–585.

SANTHOSH, R. & BASU, S. 2015 Acoustic response of vortex breakdown modes in a coaxial isothermal unconfined swirling jet. *Phys. Fluids* **27**, 033601.

SANTHOSH, R., MIGLANI, A. & BASU, S. 2013 Transition and acoustic response of recirculation structures in an unconfined co-axial isothermal swirling flow. *Phys. Fluids* **25**, 083603.

SANTHOSH, R., MIGLANI, A. & BASU, S. 2014 Transition in vortex breakdown modes in a coaxial isothermal unconfined swirling jet. *Phys. Fluids* **26**, 043601.

SARPKAYA, T. 1971*a* Vortex breakdown in swirling conical flows. *AIAA J.* **9**, 1792–1799.

SARPKAYA, T. 1971*b* On stationary and travelling vortex breakdowns. *J. Fluid Mech.* **45**, 545–559.

SARPKAYA, T. 1974 Effect of the adverse pressure gradient on vortex breakdown. *AIAA J.* **12**, 602–607.

SCHMID, P. J. 2010 Dynamic mode decomposition of numerical and experimental data. *J. Fluid Mech.* **656**, 5–28.

SCIACCHITANO, A., WIENEKE, B. & SCARANO, F. 2013 PIV uncertainty quantification by image matching. *Meas. Sci. Technol.* **24**, 045302.

SIROVICH, L. 1987 Turbulence and the dynamics of coherent structures. Part I. Coherent structures. *Q. Appl. Maths* **45**, 561–571.

SPALL, R. E., GATSKI, T. B. & GROSCH, C. E. 1987 A criterion for vortex breakdown. *Phys. Fluids* **30**, 3434–3440.

STEINBERG, A. M., BOXX, I., STÖHR, M., MEIER, W. & CARTER, C. D. 2012 Effects of flow structure dynamics on thermoacoustic instabilities in swirl-stabilized combustion. *AIAA J.* **50**, 952–967.

STÖHR, M., ARNDT, C. M. & MEIER, W. 2013 Effects of Damköhler number on vortex–flame interaction in a gas turbine model combustor. *Proc. Combust. Inst.* **34**, 3107–3115.

STÖHR, M., ARNDT, C. M. & MEIER, W. 2015 Transient effects of fuel–air mixing in a partially-premixed turbulent swirl flame. *Proc. Combust. Inst.* **35**, 3327–3335.

SYRED, N. 2006 A review of oscillation mechanisms and the role of the precessing vortex core (PVC) in swirl combustion systems. *Prog. Energy Combust. Sci.* **32**, 93–161.

TAIRA, K., BRUNTON, S. L., DAWSON, S., ROWLEY, C. W., COLONIUS, T., MCKEON, B. J., SCHMIDT, O. T., GORDEYEV, S., THEOFILIS, V. & UKEILEY, L. S. 2017 Modal analysis of fluid flows: an overview. arXiv:1702.01453.

WANG, S., RUSAK, Z., GONG, R. & LIU, F. 2016 On the three-dimensional stability of a solid-body rotation flow in a finite-length rotating pipe. *J. Fluid Mech.* **797**, 284–321.

WIENEKE, B. 2015 PIV uncertainty quantification from correlation statistics. *Meas. Sci. Technol.* **26**, 074002.

WILLIAMS, M. O., KEVREKIDIS, I. G. & ROWLEY, C. W. 2015 A data-driven approximation of the Koopman operator: extending dynamic mode decomposition. *J. Nonlinear Sci.* **25**, 1307–1346.

WILSON, B. M., MEJIA-ALVAREZ, R. & PRESTRIDGE, K. 2015 Simultaneous PIV and PLIF measurements of Mach number effects on single-interface Richtmyer–Meshkov mixing. In *29th International Symposium on Shock Waves 2*, pp. 1125–1130. Springer.